# Dynamic recrystallization behavior under inhomogeneous thermomechanical deformation state

Yan Peng, Shicheng Liang, Caiyi Liu, Silvia Barella, Shuo Guo, Andrea Gruttadauria, Marco Belfi, Yang Liu, Xiaobo Qu, Carlo Mapelli

# Dynamic recrystallization behavior under inhomogeneous thermomechanical deformation state

Yan Peng[1,*], Shicheng Liang[1], Caiyi Liu[1], Silvia Barella[2], Shuo Guo [1], Andrea Gruttadauria[2], Marco Belfi[2], Yang Liu, Xiaobo Qu, Carlo Mapelli[2]

1. National Engineering Research Center for Equipment and Technology of Cold Strip Rolling, Yanshan University, Qinhuangdao 066004, China

2. Department of Mechanical Engineering, Politecnico di Milano, Milan, 20156, Italy

3. Product Research Development Center Jiangsu Yonggang Group Co.Ltd, Zhangjiagang, 215600, China

* Correspondence: pengyan@ysu.edu.cn

**Abstract**: Dynamic recrystallization (DRX) is of great significance for refining grains, improving mechanical properties, and obtaining high-quality products during thermomechanical deformation. This paper studies the DRX behavior of low carbon steel within the temperature range of 900°C~1100°C and the strain rate of $0.01s^{-1}$~$1s^{-1}$ based on the Gleeble-3800 thermal-simulation experimental machine and establishes a DRX kinetic model suitable for different strain rates. The established model is embedded in the DEFORM-3D simulation software to simulate the DRX behavior of high-temperature plastic deformation of the material and to study the influence of the deformation amount, deformation temperature and strain rate on the deformation inhomogeneity of the material. The results show that under the strain rate of $0.01s^{-1}$, the 2/5 position from center to surface corresponds to the preset strain, and under the strain rate of $0.1s^{-1}$~$1s^{-1}$, the 1/2 position from center to surface corresponds to the preset strain, and the importance of the sampling position is proved in combination with the DRX behavior. This paper establishes a sampling theory that describes the position corresponding to the preset deformation amount, and it is important for guiding subsequent microstructural characterization experiments to reveal the DRX behavior of materials during thermomechanical deformation.

Keywords: thermomechanical deformation; Dynamic recrystallization; Deformation inhomogeneity; Physical simulation; Numerical simulation

## 1. Introduction

In the process of thermomechanical deformation of metal materials, dynamic recrystallization is a critical mechanism of microstructure evolution, and a detailed understanding of the entire process is helpful to determine the optimal forming conditions for materials [1-3]. The high-temperature deformation experiment of metal samples by thermal simulation experimental machine provides data support for establishing the constitutive and dynamic recrystallization models. It is a common method to analysis materials' microstructure and mechanical properties in actual forging, rolling and thermomechanical treatment [4-6]. The flow behavior of materials during thermal deformation is complex. Both hardening and softening processes are significantly affected by temperature and strain rate[7]. An in-depth understanding of the flow behavior of metals and alloys under hot deformation conditions has important implications for the design of thermomechanical machining.Therefore, the functional relationship among flow stress, deformation temperature, and strain rate during high temperature deformation needs to be determined by the constitutive model. At present,the Johnson-Cook model[8] and the Arrhenius model[9] are representatives.These models have the advantages of less material constants, convenient use, and are suitable for practical production applications. It is the research method that most scholars prefer in recent years. The Johnson-Cook constitutive model is mainly used in engineering fields such as explosion,impact and stamping under large strain, high

strain rate, and high-temperature environment. The Arrhenius model is suitable for most metal materials under high-temperature deformation,and has high accuracy. Qian et al. [10] established the Advanced Ma-Wang model for the extreme deformation process in the cold spraying process, considering the joint effects of thermal activation and dislocation resistance mechanisms, which can predict the flow behavior of materials when the strain rate is less than $10^9$. The constitutive model plays an important role in describing the flow behavior of materials. Each constitutive model has its corresponding applicable environment, and the appropriate constitutive model can be better predicted according to the different research contents. For dynamic recrystallization, by calculating the work hardening rate of 300M steel, Li et al. determined the critical strain for dynamic recrystallization, studied the effect of temperature on the dynamic recrystallization process, and established the corresponding kinetic equation [11]. Chen et al. studied the dynamic recrystallization (DRX) behavior in 42CrMo steel through physical simulation experiments, discussed the effects of deformation temperature, strain rate and initial austenite grain size on the dynamic recrystallization behavior, and established the DRX kinetic equations to predict DRX-induced softening behavior [12]. Wang et al. studied the DRX behavior of Inconel 740 superalloy through isothermal compression experiments and constitutive models and obtained the evolution law of flow stress, grain size and DRX fraction during hot deformation at constant strain rate [13]. Considering the influence of temperature, strain and strain rate on the flow stress of Nb-containing 316LN material, Li et al. established an improved Arrhenius constitutive model and combined OM, EBSD, TEM and other characterization methods to clarify the microstructure evolution and dynamic recrystallization mechanism of the material [14]. Xu et al. determined the activation energy of DRX and Z parameters by regression analysis of X70 steel stress-strain data and modified the Avrami model [15]. Chen et al. created a DRX kinetic model of 40Cr steel based on uniform deformation conditions through a modified Avrami model [16].Wu et al. studied the DRX nucleation mechanism and microstructure evolution law of FGH96 high-temperature alloy during hot compression based on experimental data and microstructure characterization and analyzed the effect of deformation conditions on the strain and DRX distribution of hot forged samples by combining numerical simulation techniques [17].

In the actual thermomechanical deformation process, the friction between the contact surface of the indenter and the sample changes the unidirectional compressive stress state leading to a bulging state of the sample, i.e., the phenomenon of deformation inhomogeneity, resulting in large differences in the microstructural characterization and mechanical properties at different locations of the sample. Existing studies in microstructural characterization when the observation surface is taken directly from the center of the compressed sample cannot accurately reflect the actual situation [18-20]. Therefore, it is important to clarify the error between the actual deformation conditions of the physical simulation and the preset deformation conditions for the accuracy of the physical simulation.

With the continuous development of numerical simulation technology, it has been widely used in thermomechanical processes in recent years. Embedding the intrinsic structure model based on physical simulation into numerical simulation can provide a theoretical basis for designing and optimizing the hot deformation process [21-23]. Ji et al. established a dynamic recrystallization model based on the JMAK model through the flow stress curve of 33Cr23Ni8Mn3N steel. The results of the compressed samples' longitudinal section central microstructural characterization were compared with the numerical simulation results for verification [24]. Zhao et al. analyzed the distribution of effective strain and strain rate on the longitudinal section of the sample after deformation by numerical simulation method to reveal the quantitative relationship between effective strain, strain rate and preset strain in the surface and center [25]. Sui et al. considered the influence of the height-diameter

ratio of the sample on the deformation uniformity. They found a height-diameter ratio favorable for metallographic experiments [26]. Ye et al. analyzed the effect of the friction coefficient between the indenter and the sample on the degree of deformation inhomogeneity by numerical simulation methods, revealing that different friction coefficients have little effect on the location on the central axis of the longitudinal section of the sample equal to the preset strain [27]. Although there have been some publications on the study of sampling methods for physical simulations in recent years, these studies have not considered the effect of theoretical and practical sampling locations on the dynamic recrystallization of materials under the combined effects of different deformation amounts, deformation temperatures and strain rates.

In this article, based on the results of physical simulation experiments, the strain rate is considered to describe in different stages to optimize the DRX kinetic model. The effects of different deformation amounts, deformation temperatures and strain rates conditions on the strain distribution of the experimental steel are studied by numerical simulation methods. Combined with the dynamic recrystallization volume fraction in the corresponding cross-section zone, the gap between the actual sampling location and the theoretical sampling location of the physical simulation process is clarified, which can provide theoretical guidance for material physical simulation, microstructural characterization and performance evaluation.

## 2. Experimental procedures

The experimental material in this paper comes from a commercial hot-rolled low-carbon steel strip. The chemical composition of the experimental steel is shown in Table 1. The φ10×15mm cylindrical sample was processed from the hot-rolled strip by wire cutting method. The single-pass hot compression experiment was performed using a Gleeble-3800 thermal-simulation experimental machine. Before the start of the experiment, the sample needs to be ground and polished to ensure surface smoothness, and a K-type thermocouple is welded to the sample's axial center to measure the sample's temperature change law during the experiment. Due to the increase of friction between the contact surface between the sample and the indenter during the hot compression process, the difficulty of metal flow on the sample's surface is increased, resulting in deformation inhomogeneity and expansion. To reduce the effect of friction on the stress state, tantalum sheets coated with molybdenum disulphide high-temperature lubricant were placed at both ends of the sample. Inserting a graphite sheet enhances the conductivity, makes the temperature of the sample axis uniform and eliminates the axial temperature gradient.

The hot compression experiments are as follows: all samples are heated to 1150℃ and held for 3 min at a heating rate of 10℃/s in a high-purity argon atmosphere to obtain a uniform austenite structure. Samples are then cooled to the deformation temperature at a rate of 5℃/s and held for 60 s to eliminate the temperature gradient. All samples are deformed by 55% at four different strain rates ($0.01s^{-1}$, $0.1s^{-1}$, $0.5s^{-1}$ and $1s^{-1}$), corresponding to a true strain of 0.8. Finally, samples are quenched and cooled to room temperature. The Gleeble-3800 thermal-simulation experimental machine automatically saves the material stress-strain experimental data, and the specific experimental procedure is shown in Fig. 1.
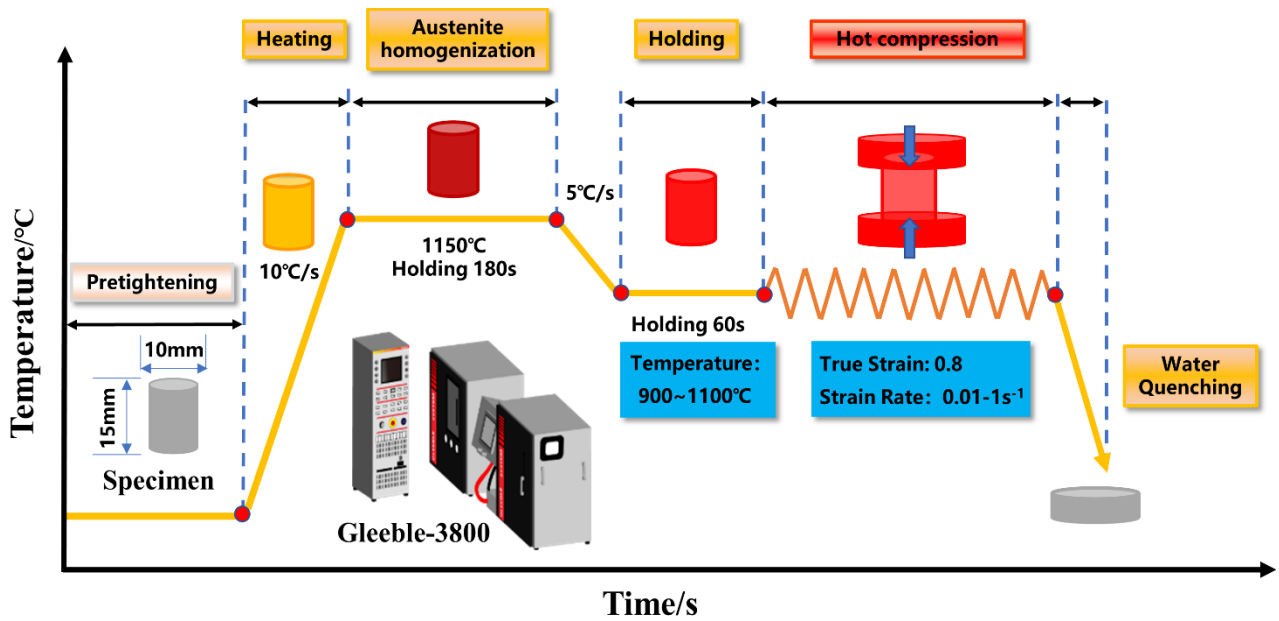
**Fig.1.** Experimental procedure.

**Table 1.** Chemical composition of the experimental steel (wt.%)

| C | Si | Mn | P | S | Cr | Ni | Mo | N | Fe |
|---|-----|------|-------|-------|------|-------|------|-------|------|
| 0.023 | 0.59 | 1.49 | 0.027 | 0.001 | 16.7 | 10.13 | 2.05 | 0.035 | bal. |

## 3. Result and discussion

### 3.1 DRX behavior analysis

#### 3.1.1 The flow stress curve analysis

The flow stress curves from different deformation conditions are obtained through experiments, as shown in Fig. 2. Under the strain rate of $0.01s^{-1}$ and $0.1s^{-1}$, the flow stress curve shows significant peak within the deformation temperature range of 900℃~1100℃, indicating that the material occurred significant dynamic softening behavior during hot compression, and the peak stress and peak strain increased with the decrease of deformation temperature. With the gradual increase of strain rate, the dynamic softening behavior requires higher deformation temperature conditions.
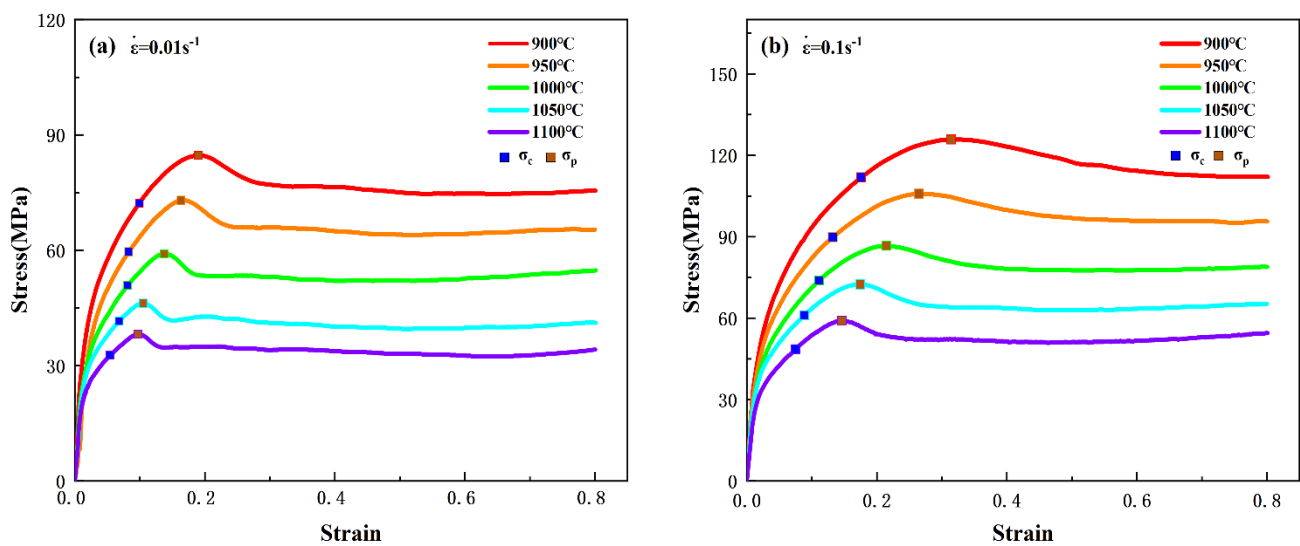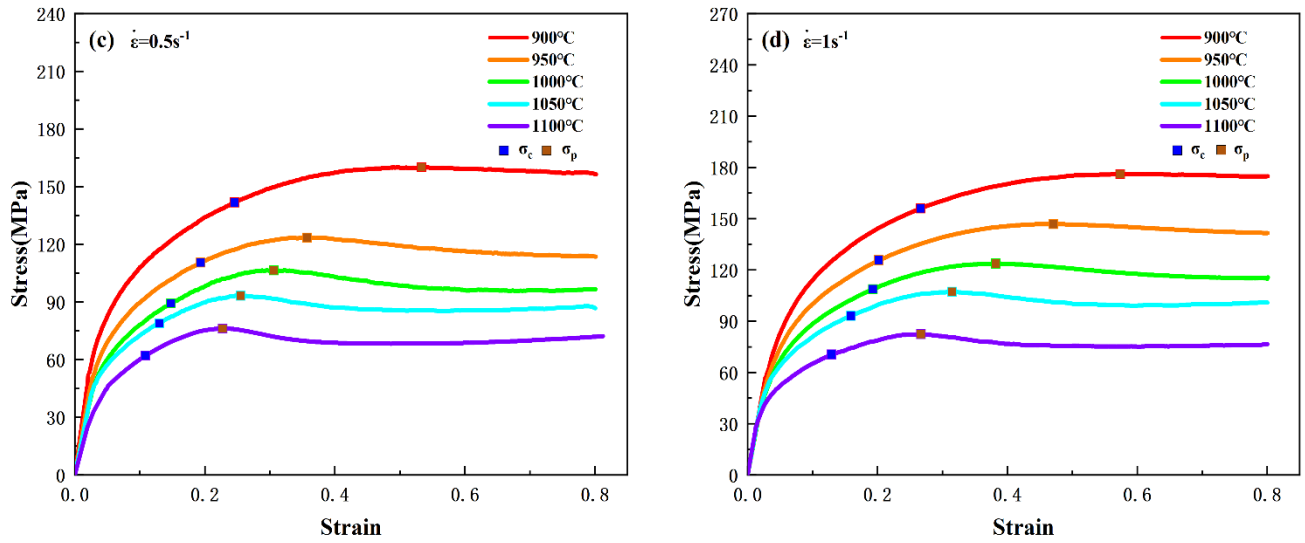
**Fig. 2.** Flow stress curves at different strain rates: (a) $0.01s^{-1}$, (b) $0.1s^{-1}$, (c) $0.5s^{-1}$, (d) $1s^{-1}$.

*3.1.2 DRX critical condition*

This study adopted the method of determining the critical point of DRX proposed by Poliaki and Jonas [28-30]. At the beginning of deformation, the work hardening rate decreases linearly with increasing stress. With the increase of stress, the material undergoes dynamic recovery, which leads to a gradual flattening of the work-hardening rate under the combined effect of dynamic reversion softening and work-hardening. An inflection point appears in the work hardening rate θ - stress σ curve, which is the critical point for dynamic recrystallisation (σ=σ$_c$). The stress at the critical point is defined as the critical stress where dynamic recrystallization occurs, and its corresponding strain on the flow stress curve is the critical strain ε$_c$. Fig. 3 shows the work hardening rate curves at different strain rates.s at different strain rates.The position of the corresponding inflection point in the work hardening rate θ-stress σ curve is the critical point where work hardening begins to change to dynamic softening, and the stress at the critical point is defined as the critical stress where dynamic recrystallization occurs, and its corresponding strain on the flow stress curve is the critical strain $\varepsilon_c$. Fig. 3 shows the work hardening rate curves at different strain rates.
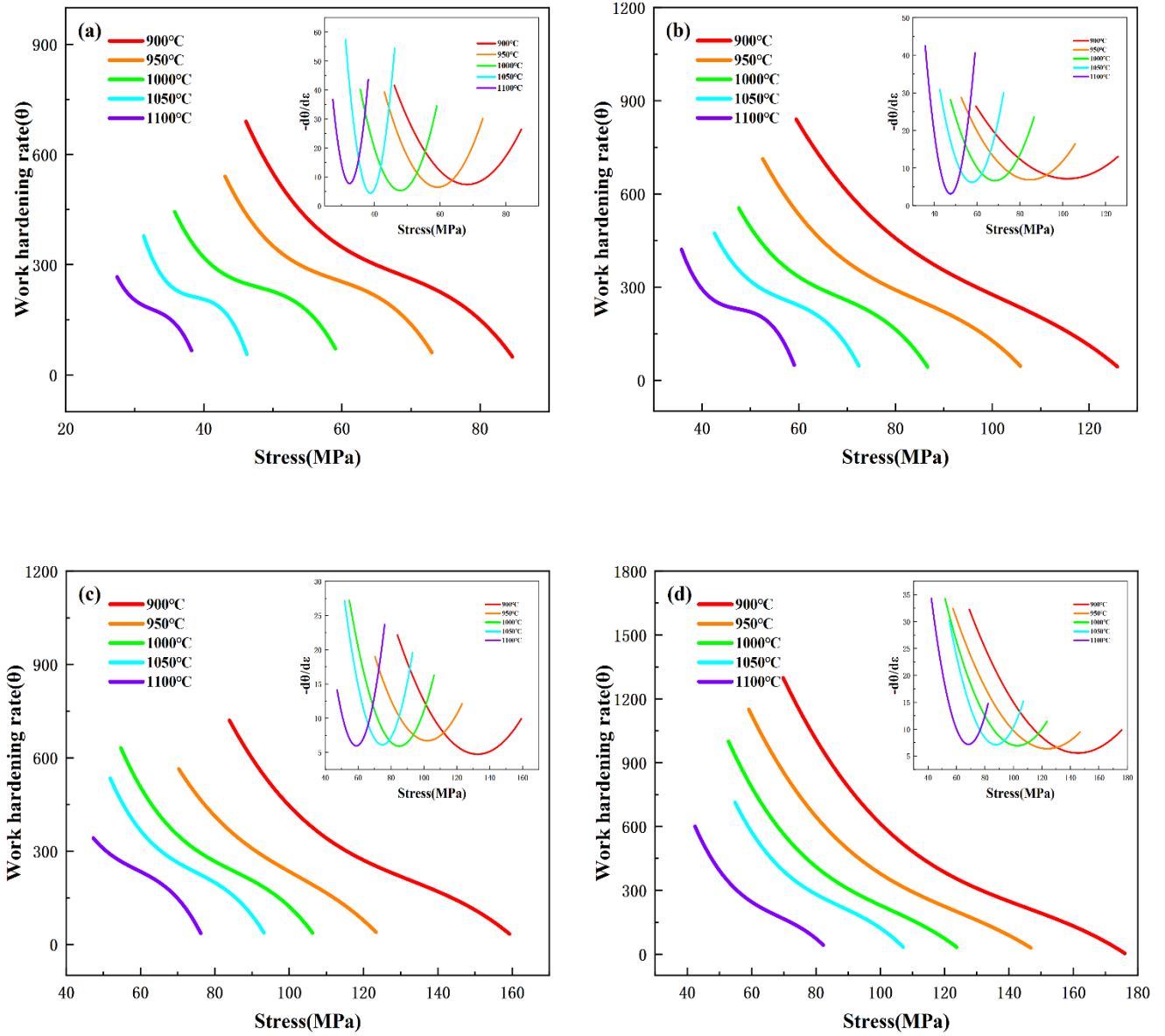
**Fig.3.** Work hardening rate curves at different strain rates: (a) $0.01s^{-1}$, (b) $0.1s^{-1}$, (c) $0.5s^{-1}$, (d) $1s^{-1}$.

Fig. 4 shows the critical strain $\varepsilon_c$ and the peak strain $\varepsilon_p$ under different deformation conditions. It can be analyzed that the critical strain $\varepsilon_c$ and the peak strain $\varepsilon_p$ decrease with the decrease of strain rate and the increase of deformation temperature. It is also verified that low strain rate and high deformation temperature can promote the occurrence of DRX behavior. It can be seen from Fig. 5 that there is a linear relationship between them: $\sigma_c = 0.846\sigma_p$, $\varepsilon_c = 0.33\varepsilon_p$.
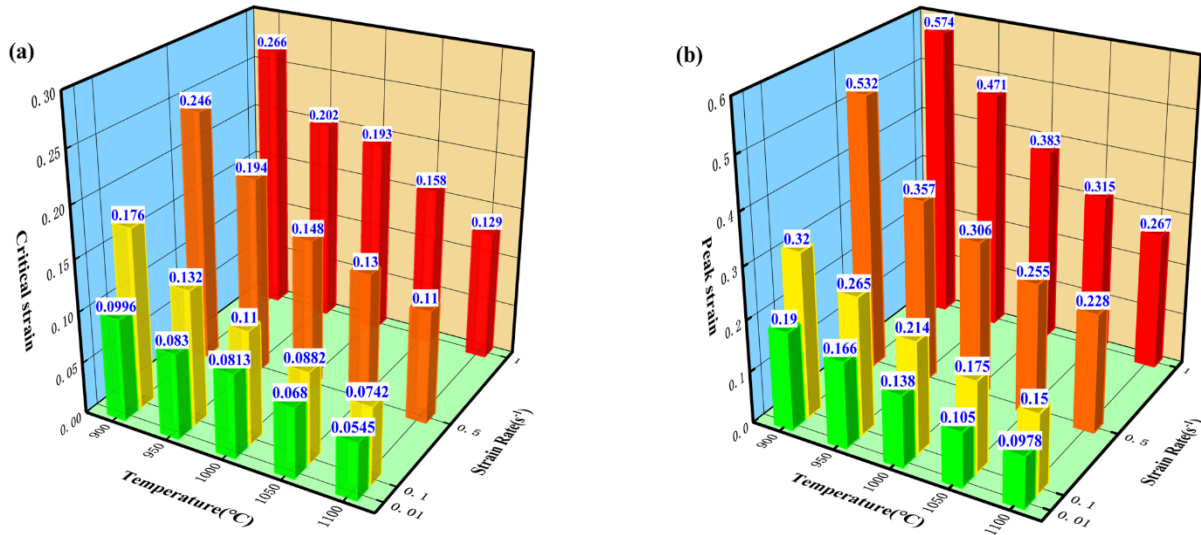
**Fig.4.** Characteristic parameters of DRX behavior of materials under different deformation conditions: (a) critical strain $\varepsilon_c$, (b) peak strain $\varepsilon_p$.
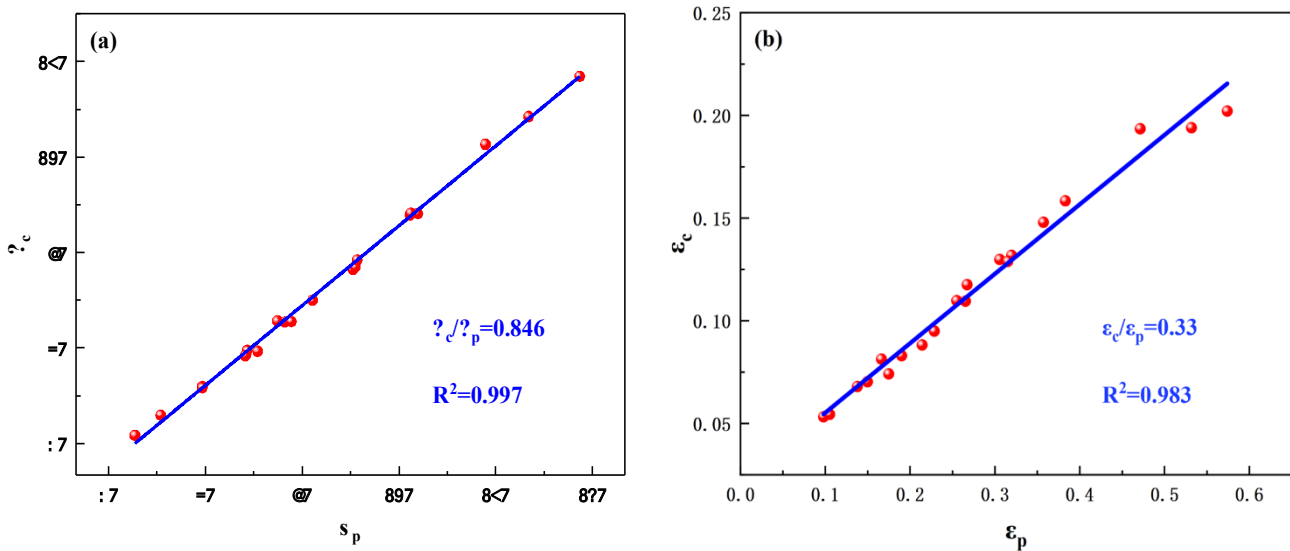


**Fig. 5.** (a): Linear relationship between critical stress $\sigma_c$ and peak stress $\sigma_p$, (b): Linear relationship between critical strain $\varepsilon_c$ and peak strain $\varepsilon_p$.

### 3.1.3 Zener-Hollomon model

An in-depth understanding of the rheological behaviour of metals under thermal deformation conditions is important for the design of thermal processing processes. The constitutive model is a function of the rheological stresses in the high temperature deformation process and the deformation temperature and strain rate, which can describe the basic information of the thermal deformation process of metallic materials and provide theoretical guidance for the actual thermal processing process, thus improving the organisation and properties of materials.

Under the condition of high-temperature plastic deformation, the relationship between flow stress, strain rate and temperature can be expressed by the hyperbolic sine form of hot deformation activation energy $Q$ and temperature $T$ proposed by Sellars and Tegart [30-33] :

$$\dot{\varepsilon} = AF(\sigma) \, exp\left(-\frac{Q}{RT}\right) \quad (1)$$

where $F(\sigma)$ has three forms under different stress conditions, as shown in Equation 2.

$$F(\sigma) = \begin{cases} \sigma^{n_1} \, (\alpha\sigma < 0.8) \\ exp(\beta\sigma) \, (\alpha\sigma \geq 1.2) \\ [sin(\alpha\sigma)]^n \, (all \; conditions) \end{cases} \quad (2)$$

where $\sigma$ is the stress, $Q$ is the activation energy of hot deformation, which reflects the difficulty of dynamic recrystallization during thermomechanical deformation of the material, $R$ is the gas constant（$8.314 J \cdot mol^{-1} \cdot K^{-1}$）, and $T$ is the deformation temperature. $A$、$n_1$、$\beta$、$n$ are constants related to the material.

The Zener-Hollomon equation can describe the relationship between strain rate and temperature [34,35]:

$$Z = \dot{\varepsilon} \, exp\left(\frac{Q}{RT}\right) = A[sin(\alpha\sigma_P)]^n \quad (3)$$

Substituting Equation 2 into Equation 1 and taking the natural logarithm for both sides of the equation, the following equation can be obtained

$$ln\dot{\varepsilon} = lnA_1 + n_1 ln\sigma_P - \frac{Q}{RT} \quad (4)$$

$$ln\dot{\varepsilon} = lnA_2 + \beta\sigma_P - \frac{Q}{RT} \quad (5)$$

$$ln\dot{\varepsilon} = lnA + nln[sin(\alpha\sigma_P)] - \frac{Q}{RT} \quad (6)$$

The $ln\dot{\varepsilon} - ln\sigma_P$ and $ln\dot{\varepsilon} - \sigma_P$ curves are plotted, as shown in Fig. 6 (a), (b). $n_1$ and $\beta$ can be obtained by linear fitting. The stress level coefficient $\alpha \approx \frac{\beta}{n_1}$ =0.01058. Differentiating Equation 6, $Q$ can be expressed as:

$$Q = Rn\frac{\partial ln[sin(\alpha\sigma_P)]}{\partial 1/T} \quad (7)$$

$$n = \frac{\partial ln\dot{\varepsilon}}{\partial ln[sin(\alpha\sigma_P)]} \quad (8)$$

By performing linear fitting on $ln\dot{\varepsilon} - ln[sin(\alpha\sigma_P)]$ at different deformation temperatures, the value of $n$ is obtained as 4.962, and by linear fitting on $ln[sin(\alpha\sigma_P)] - 1/T$, the thermal deformation activation energy $Q = 311.729 KJ/mol$, there is a linear relationship between $lnZ$ and $\ln[sin(\alpha\sigma_P)]$, as shown in Fig. 7, with an intercept of $lnA$, so $A$ can be obtained as $1.23 \times 10^{12}$. Therefore, the constitutive equation of the thermal deformation of the material is expressed as:

$$\dot{\varepsilon} = 1.23 \times 10^{12} [sinh(0.01058\sigma)]^{4.962} \, exp\left(\frac{-311729}{RT}\right) \quad (9)$$
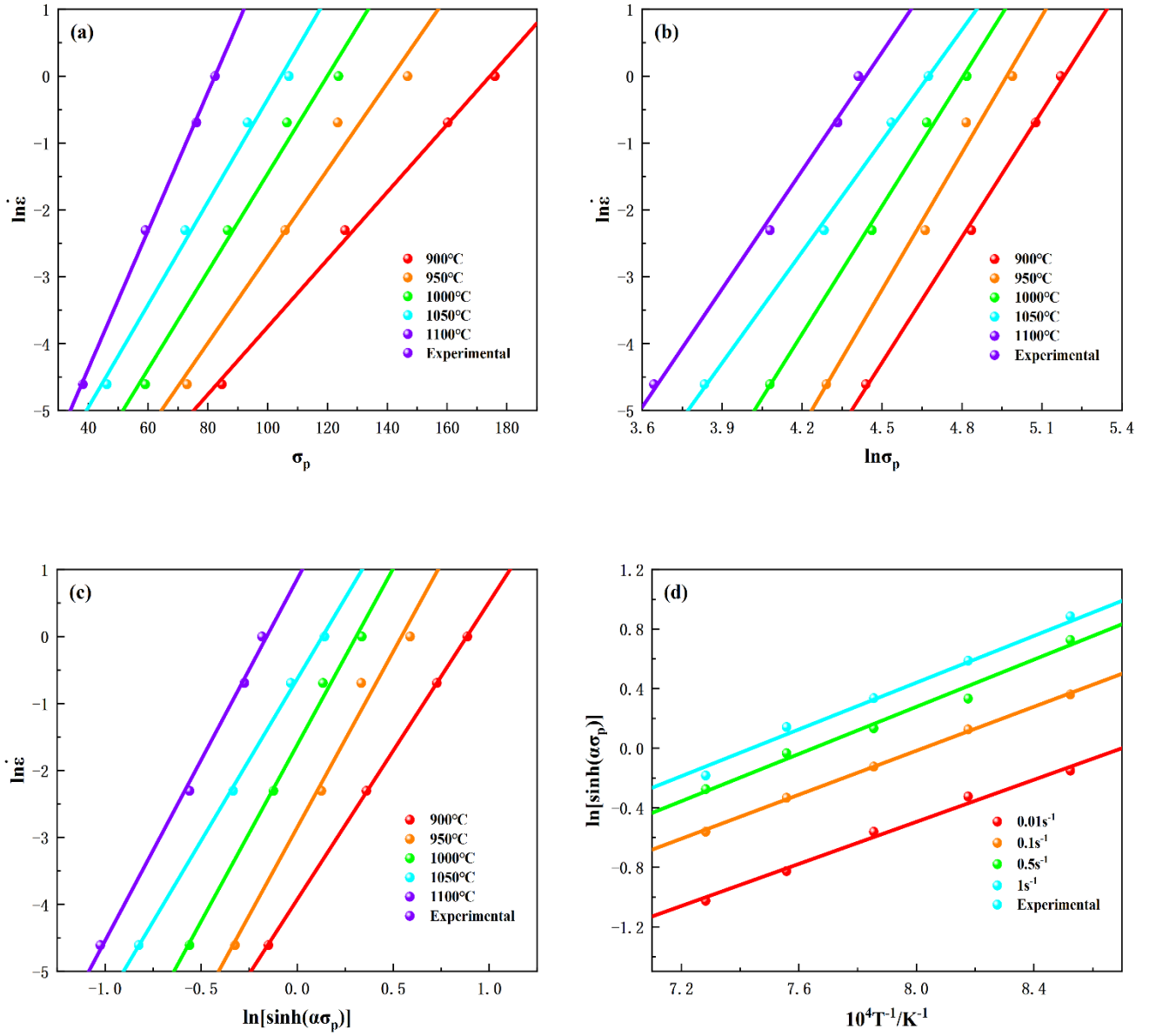
**Fig. 6.** Material constants and activation energy of deformation calculation: (a) $ln\dot\varepsilon - ln\sigma_P$, (b) $ln\dot\varepsilon - \sigma_P$, (c) $ln\dot\varepsilon - ln[sin(\alpha\sigma_P)]$, (d) $ln[sin(\alpha\sigma_P)] - T^{-1}$.
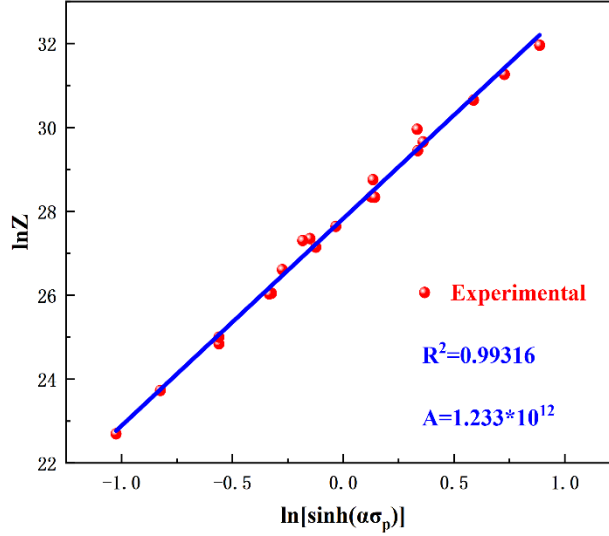
**Fig. 7.- Relationship between peak stress $\sigma_P$ and Zener-Hollomon parameters.**

According to related studies [36,37], the characteristic parameters of material DRX behavior (critical stress $\sigma_c$, critical strain $\varepsilon_c$, peak stress $\sigma_p$, peak strain $\varepsilon_p$) are quantitatively related to the strain rate and deformation temperature based on the Zener-Hollomon model. $\varepsilon_c = 1.21905 \times 10^{-4}Z^{0.16168}$, $\varepsilon_p = 1.00704 \times 10^{-4}Z^{0.19884}$。

*3.1.4 DRX kinetic model*

Quantitatively describing the change process of dynamic recrystallization from occurrence to completion is important to accurately calculate the dynamic recrystallization volume fraction. This paper uses the optimized John J. Jonas model to describe the dynamic recrystallization volume fraction [38, 39].

$$X_{DRX} = \frac{\sigma_{recov} - \sigma}{\sigma_{sat} - \sigma_{ss}} \quad (10)$$

Where $X_{DRX}$ is the dynamic recrystallization volume fraction, $\sigma_{recov}$ is the dynamic recovery pressure, $\sigma$ is the flow stress, $\sigma_{sat}$ is the dynamic recovery saturation stress, and $\sigma_{ss}$ is the steady-state stress. Where $\sigma$, $\sigma_{ss}$ and $\sigma_{sat}$ can be obtained from experimental data. $\sigma_{recov}$ can be obtained from equation (11):

$$\sigma_{recov} = \sqrt{\sigma_{sat}^2 - (\sigma_{sat}^2 - \sigma_i^2)exp\,(-r\varepsilon)}(11)$$

$\sigma_i$ is the stress value between the experimental material's initial stress and critical stress, and $r$ is the dynamic recovery coefficient. The dynamic recovery curve is the softening behavior under the combined action of work hardening and dynamic recovery. Before the critical strain, the material undergoes the process of work hardening and dynamic recovery. Therefore, between the initial strain and the critical strain, the dynamic recrystallization and dynamic recovery curves are the same, and the dynamic recovery coefficient $r$ can be obtained from equation (12):

$$r\varepsilon = ln\,(\frac{\sigma_{sat}^2 - \sigma_i^2}{\sigma_{sat}^2 - \sigma_{recov}^2})(12)$$

The linear relationship between $\varepsilon$ and $ln\,(\frac{\sigma_{sat}^2-\sigma_i^2}{\sigma_{sat}^2-\sigma_{recov}^2})$ is shown in Fig. 8. The dynamic recovery coefficient $r$ is obtained from the slope of the curve.
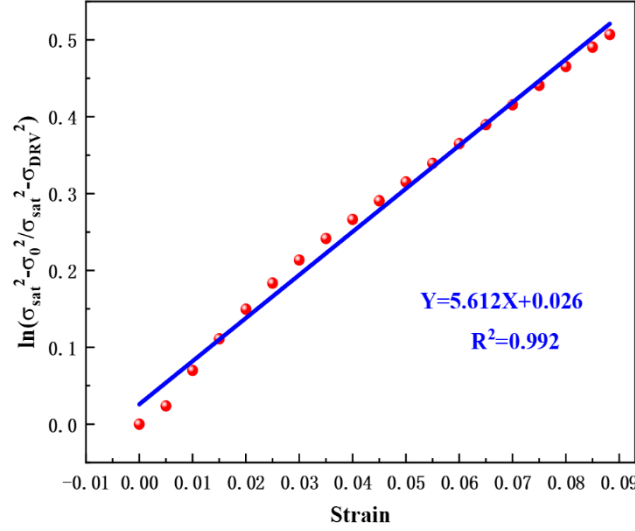
**Fig. 8.** Linear relationship between $\varepsilon$ and $ln\left(\frac{\sigma_{sat}{}^2-\sigma_i{}^2}{\sigma_{sat}{}^2-\sigma_{recov}{}^2}\right)$ at 1000℃, $1s^{-1}$.

The above method obtained the dynamic recovery stress under different experimental conditions, and the dynamic recrystallization volume fraction under the experimental conditions was calculated according to equation (13). The prediction model of DRX volume fraction under different deformation conditions based on the Avrami DRX kinetic model can be expressed as [40,41]:

$$X_{DRX} = 1 - exp\left(-b\left(\frac{\varepsilon - \varepsilon_c}{\varepsilon_p}\right)^k\right) \quad (13)$$

The constants b and k are fitting parameters. In Avrami's equation, particular assumptions regarding nucleation and growth result in exact values of these constants. Moreover, the fitting parameter soften admit interpretation in terms of the kinetic and microstructural aspects of the transformation[42] .To facilitate the fitting to determine the model, the formula is logarithmically transformed:

$$ln[-ln(1 - X_{DRX})] = lnb + kln\left(\frac{\varepsilon - \varepsilon_c}{\varepsilon_p}\right) \quad (14)$$

In previous studies, the values of b and k were usually obtained by fitting $ln[-ln(1 - X_{DRX})]$ and $ln\left(\frac{\varepsilon - \varepsilon_c}{\varepsilon_p}\right)$ at a constant strain rate to establish a DRX kinetic model and use it to approximate the DRX volume fraction at other strain rates. In order to achieve a more accurate prediction degree, $ln[-ln(1 - X_{DRX})]$ and $ln\left(\frac{\varepsilon - \varepsilon_c}{\varepsilon_p}\right)$ are fitted for different strain rates, respectively.

Then the DRX kinetic model suitable for different strain rates is established as follows：

$$X_{DRX} = \begin{cases} 1 - exp\left(-0.56\left(\dfrac{\varepsilon - \varepsilon_c}{\varepsilon_p}\right)^{1.51}\right) & (0s^{-1} < \dot{\varepsilon} \leq 0.01s^{-1}) \\[3mm] 1 - exp\left(-0.629\left(\dfrac{\varepsilon - \varepsilon_c}{\varepsilon_p}\right)^{2.01}\right) & (0.01s^{-1} < \dot{\varepsilon} \leq 0.1s^{-1}) \\[3mm] 1 - exp\left(-0.881\left(\dfrac{\varepsilon - \varepsilon_c}{\varepsilon_p}\right)^{2.31}\right) & (0.1s^{-1} < \dot{\varepsilon} \leq 0.5s^{-1}) \\[3mm] 1 - exp\left(-1.141\left(\dfrac{\varepsilon - \varepsilon_c}{\varepsilon_p}\right)^{2.608}\right) & (0.5s^{-1} < \dot{\varepsilon} \leq 1s^{-1}) \end{cases} \tag{15}$$

Fig. 9 shows the comparison between the model predicted value and the experimental value of the dynamic recrystallization volume fraction. As the deformation temperature increases and the strain rate decreases, the dynamic recrystallization volume fraction increases continuously and has a higher prediction in the range of 10% to 90%.
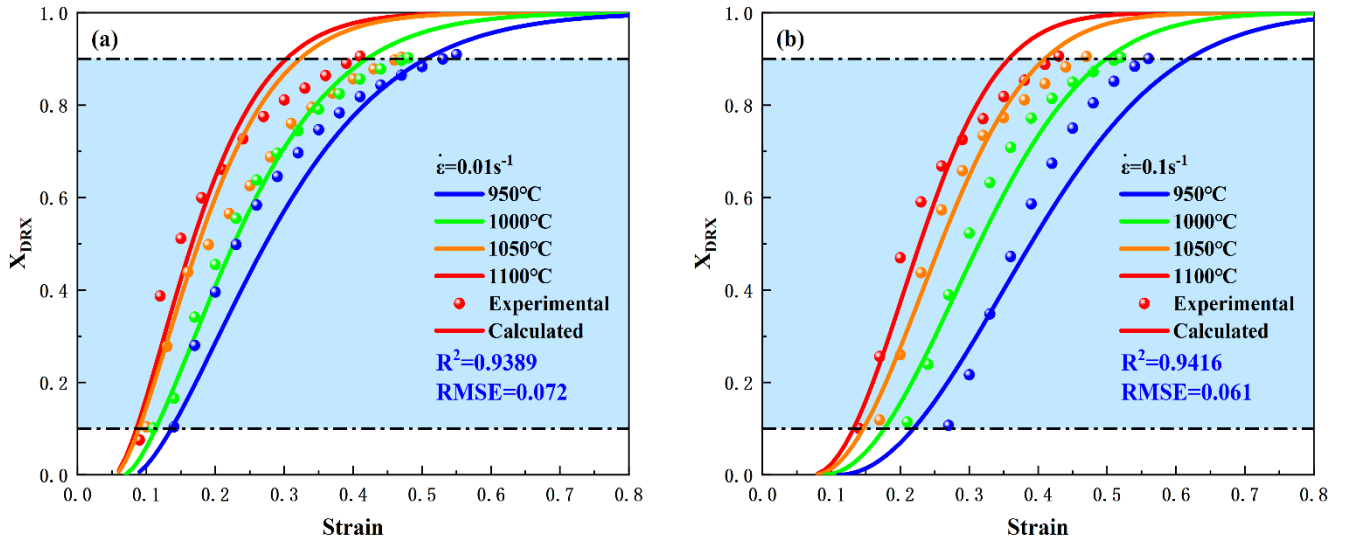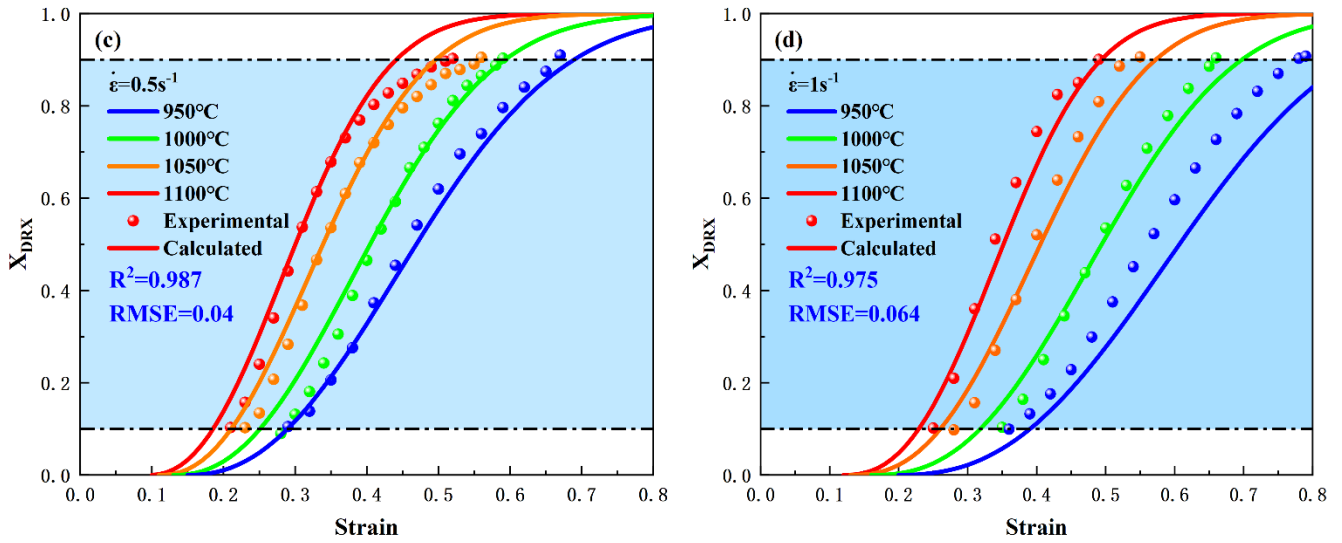
**Fig. 9.** Comparison of predicted and experimental data of the fraction of DRX at different strain rates: (a) $0.01s^{-1}$, (b) $0.1s^{-1}$, (c) $0.5s^{-1}$, (d) $1s^{-1}$.

## 3.2 Numerical simulation

### 3.2.1 Finite-element model

Finite element simulation can predict the evolution behavior of microstructure in the process of material thermomechanical processing, thus avoiding the drawbacks of the traditional trial and error method [43-45]. In this paper, DEFORM-3D software is selected for numerical simulation. In order to the accuracy of the simulation results, the hot compression deformation behavior and experiments are completed in the same environment and the boundary conditions are also consistent with the experimental process. Selecting 1/4 of the geometric model and dividing it into 16,100 brick meshes for numerical simulation can improve the calculation accuracy and save time, as shown in Fig. 10. The minimum mesh size is 0.16mm. The previously established DRX kinetic model is embedded in the DEFORM-3D software through secondary development techniques to study the change in DRX behavior of the material during hot compression. Fig. 11 shows the specific simulation flow.
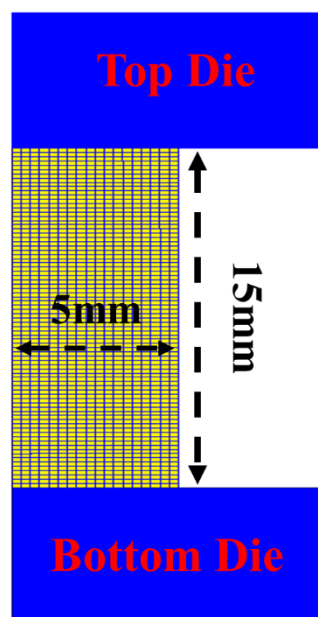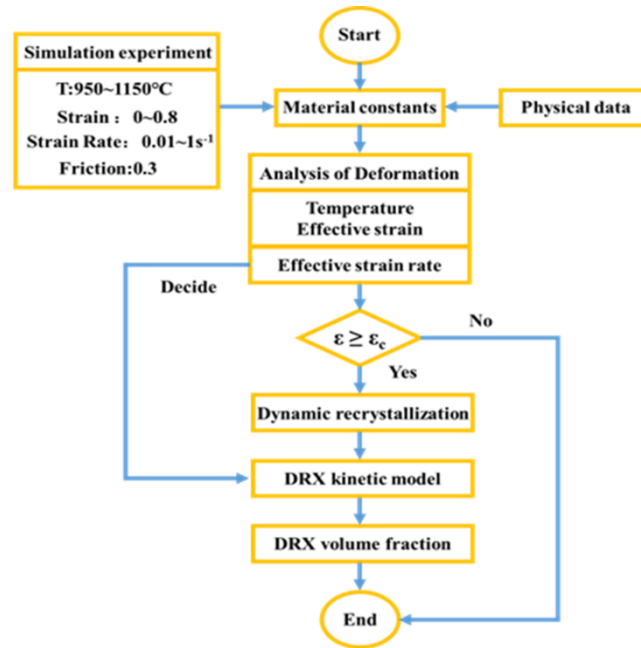
**Fig. 10.** Geometric 3D model.



**Fig. 11.** Flow chart of hot compression simulation.

*3.2.2 Basic characteristics of hot compression deformation*

During the hot compression deformation, the degree of deformation at different locations of the sample varies greatly, resulting in an extremely inhomogeneous distribution of strain.

Generally, the deformation can be divided into three zones according to the size of the deformation as shown in Fig.12: the large deformation zone (I), the difficult deformation zone (II), and the free deformation zone (III), with the degree of deformation lying between the large and difficult deformation zone [46,47].
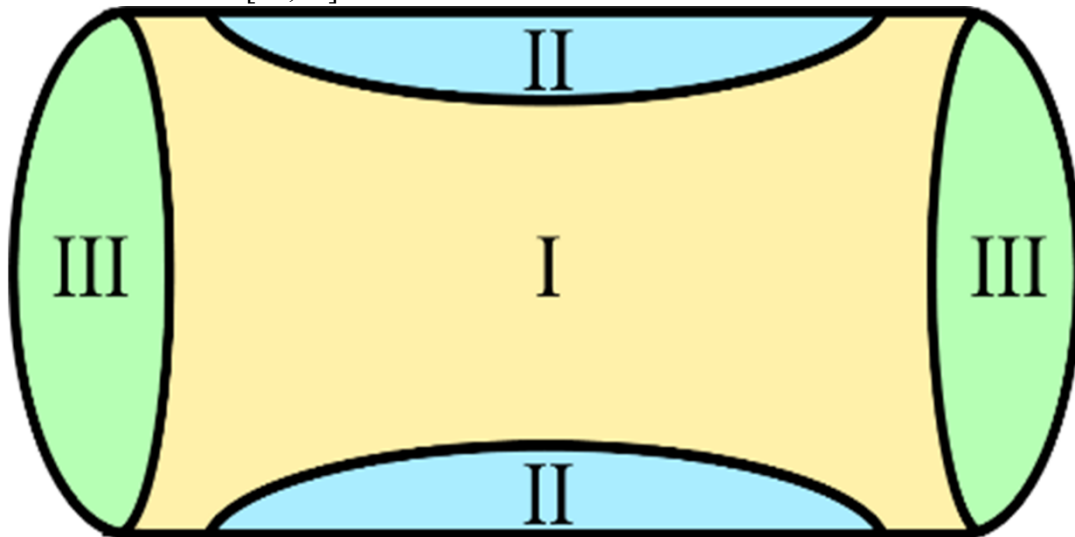


**Fig. 12.** Schematic diagram of the deformation zone of the sample.

Fig. 13(a) is the cloud graph of the strain distribution in different deformation zones under the deformation conditions of $1000℃$ and the strain rate of $0.1s^{-1}$. From the macro morphology, the sample after compression shows a drum shape. The distribution law of effective strain is consistent with the basic characteristics of thermal compression deformation, mainly manifested in two aspects: Firstly, it can be seen from Fig. 13(a) that the distribution of effective strain in the sample is not inhomogeneous under the same deformation. The value of the center of the large deformation zone

($P_1$) and surface edge is the largest, while the value of the center of the difficult deformation zone ($P_2$) is the lowest. Secondly, the point tracking technique can analyze the effective strain of each deformation zone, as shown in Fig. 13(b). With the increase of compression, the effective strain of each deformation zone increases, and the growth rate of the $P_1$ point in the large deformation zone is the fastest. The $P_2$ point in the difficult deformation zone has the slowest growth trend, and the growth range is not large，which proves that there is no obvious deformation in the difficult deformation zone. Although the effective strain increases in all zones with the increase of compression, the growth rate in general still maintains the trend of "large deformation zone > difficult deformation zone". With the increase of compression, the $P_1$ effective strain variation increases from 0 to 1.20, and the effective strain value remains the largest. This feature also confirms that the established multi-field coupled finite element model can be effectively used to predict the strain during the hot compression process. The inhomogeneous distribution characteristics of the effective strain are mainly due to the inevitable friction between the indenter and the sample. The center of the sample and the drum-shaped waist part are less effected by the friction force, and the deformation is much easier than the center of the surface.
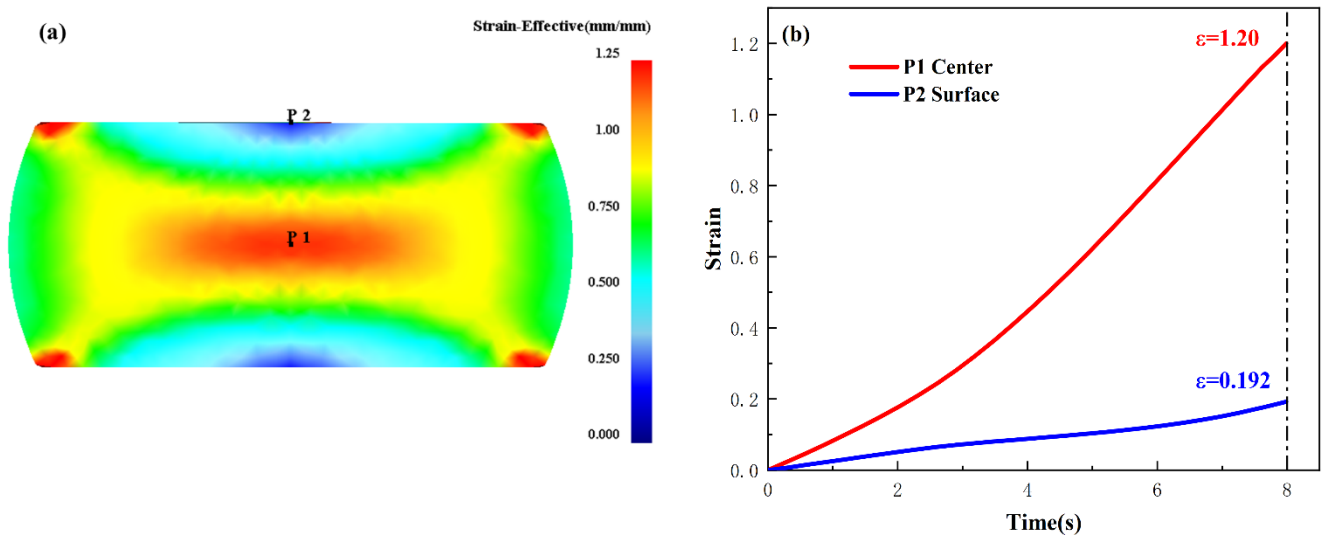


**Fig. 13.** (a) 0.8 effective strain distribution cloud graph at deformation conditions of 1000℃, $0.1s^{-1}$, (b): effective strain at the center and surface under the trace point.

*3.2.3 Effects of different deformation conditions on the dynamic recrystallization behavior of materials*

(1) Influence of deformation amount on $X_{DRX}$

Fig. 14 shows the $X_{DRX}$ simulation cloud graphs for different deformation amounts at the deformation temperature of 1000℃ and the strain rate is $0.1s^{-1}$. Fig. 15 shows the simulation curves of $X_{DRX}$ in different deformation zones obtained by the tracking point method. Based on the analysis of Fig. 14 and 15, there are significant differences in the dynamic recrystallization volume fraction for different deformation amounts. With the increase of compression, the $X_{DRX}$ in different deformation zone grows, indicating that the increase of deformation facilitates the dynamic recrystallization behavior of low carbon steel. For the respective deformation zone, the dynamic recrystallization phenomenon appears firstly in the center, and the samples' dynamic recrystallization volume fraction and effective strain distribution are consistent.

Fig. 14 shows that when the compression amount is 10%, the deformation is smaller and the dynamic recrystallization volume fraction of the sample is lower. When the compression amount further increases to 20%, the dynamic recrystallization phenomenon starts preferentially in the center, and the dynamic recrystallization volume fraction at the $P_1$ point remains the largest, mainly because the effective strain in the large deformation zone of the center is higher than the other zones. In addition, under the condition of non-external heat exchange, the centre's temperature is slightly higher than the other zones, which is more convenient for the dynamic recrystallization phenomenon. When the deformation rises to a maximum of 55%, the $X_{DRX}$ in the center of the sample reaches 100%, while the dynamic recrystallization in the surface is at a lower level of 30%.
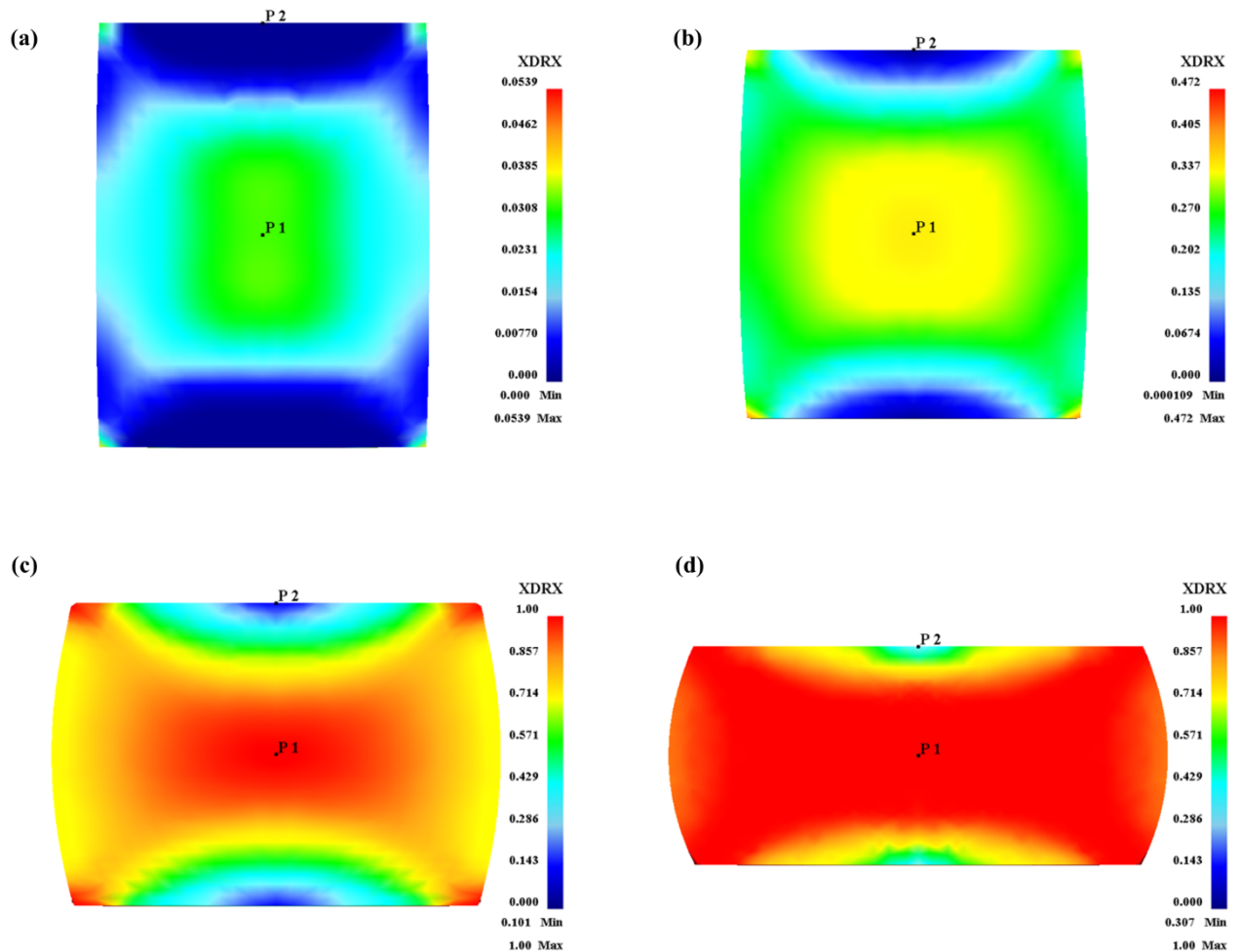


**Fig. 14.** Simulation cloud graphs of dynamic recrystallization volume fraction under different deformation amounts (1000℃, $0.1s^{-1}$): (a) ε=0.10, (b) ε=0.22, (c) ε=0.51, (d) ε=0.8.
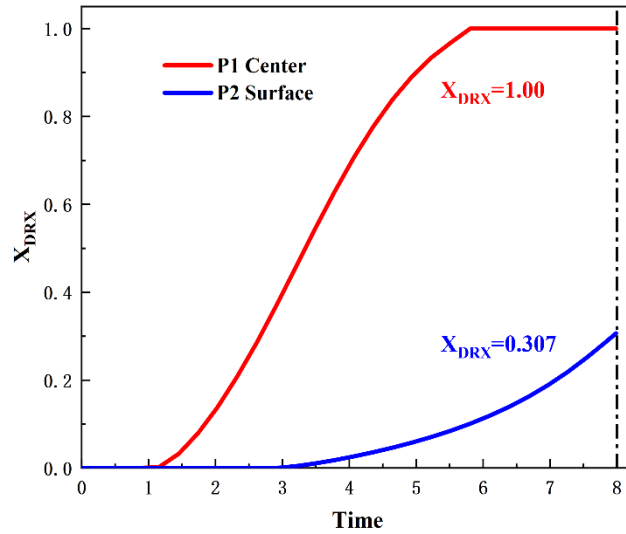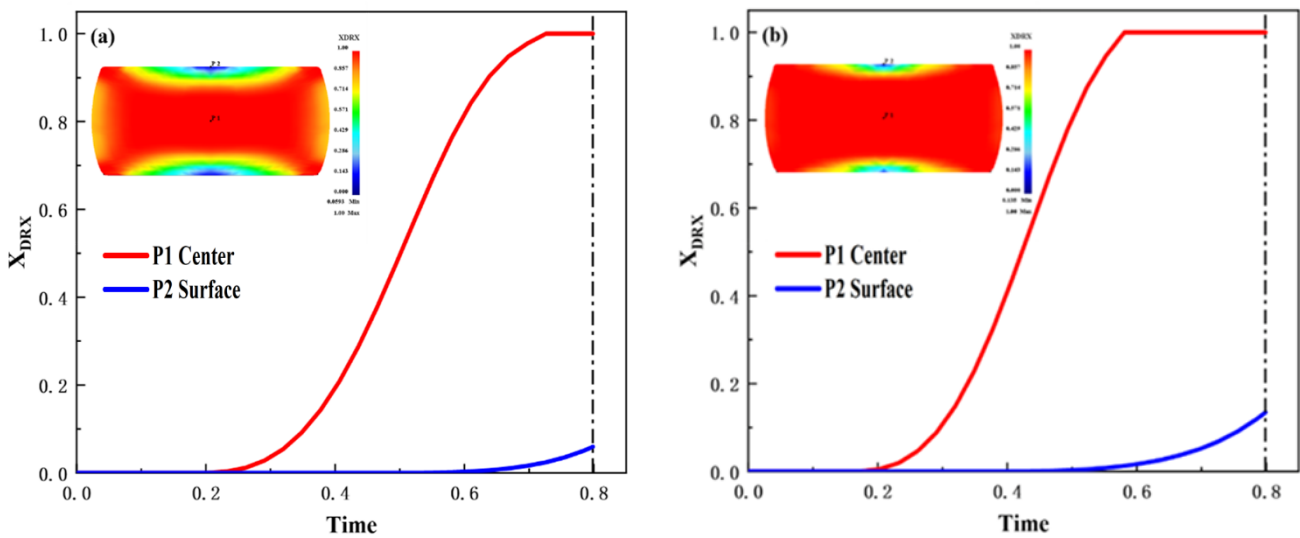
**Fig. 15.** Dynamic recrystallization volume fraction curves of tracking points in different deformation zones (1000℃, 0.1s$^{-1}$).

(2) Influence of deformation temprature on $X_{DRX}$

Fig. 16 shows the cloud diagrams and tracking point curves of $X_{DRX}$ at deformation temperature of 950℃, 1000℃, 1050℃ and 1100℃ and the strain rate of $1s^{-1}$. When the strain reaches 0.8, the samples all occur dynamic recrystallization. The dynamic recrystallization volume fraction corresponding to each deformation zone has a positive correlation property with the deformation temperature.

The simulation curves show that when the center of $X_{DRX}$ reaches 100%, the required strain gradually decreases as the temperature increases. The reason is that when the deformation amount and strain rate are constant, the increase of deformation temperature provides enough energy for the occurrence of dynamic recrystallization.
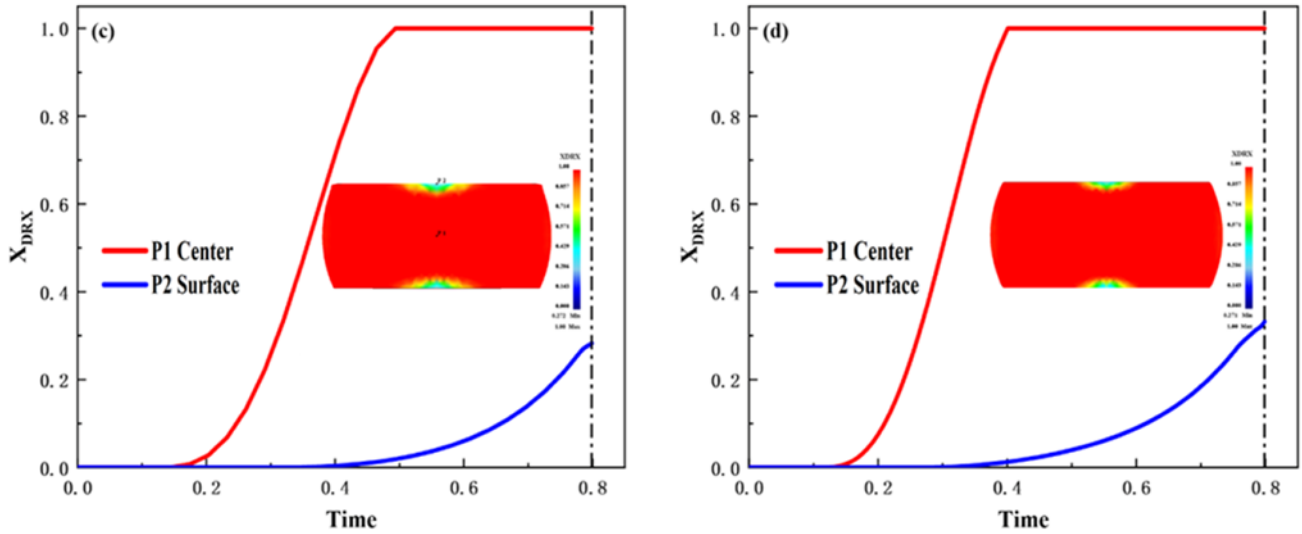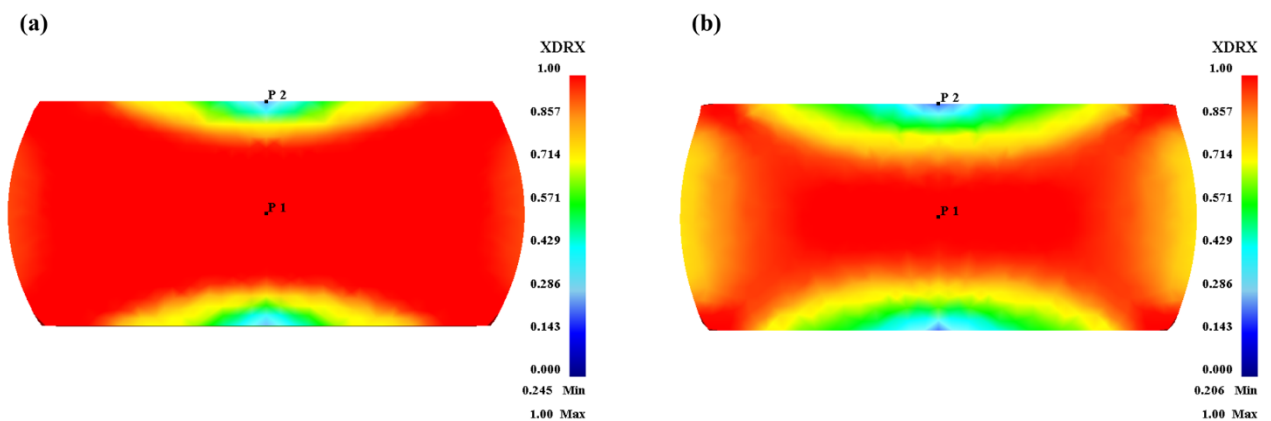
**Fig. 16.** Dynamic recrystallization volume fraction simulation graph and trace point curve at different deformation temperatures ($\varepsilon$=0.8, $\dot{\varepsilon} = 1s^{-1}$): (a) 950℃, (b) 1000℃, (c) 1050℃, (d) 1100℃.

(3) Influence of strain rate on $X_{DRX}$

Fig. 17 shows the $X_{DRX}$ simulation cloud graph under the strain rate of $0.01s^{-1}$~$1s^{-1}$ and deformation temperature of 1000℃. When the sample's strain is 0.8, $X_{DRX}$ reaches 100% at the center $P_1$ at all strain rates. The $X_{DRX}$ at the surface $P_2$ is 85.6% under the strain rate of $1s^{-1}$ and reaches 94.2% when $\dot{\varepsilon} = 0.01s^{-1}$. Therefore, a low strain rate can promote the dynamic recrystallization behavior and increase the dynamic recrystallization volume fraction.

The high strain rates increase the critical strain, making the initiation of dynamic recrystallization difficult. In addition, it takes more time to reach the same deformation amount at low strain rates, which provides a long enough time for the dynamic softening behavior.
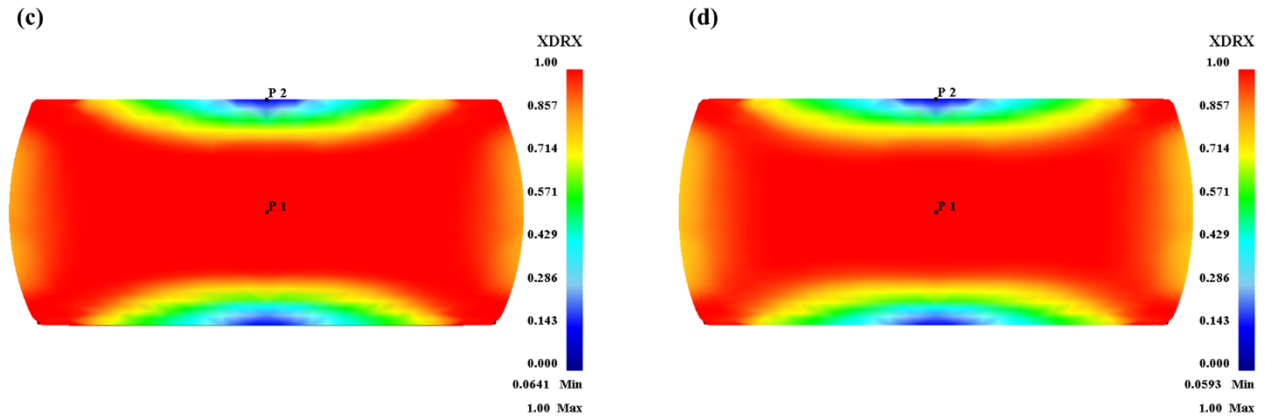
**Fig. 17.** Simulation of dynamic recrystallization volume fraction at different strain rates($\varepsilon$=0.8, 950°C): (a) $0.01s^{-1}$, (b)$0.1s^{-1}$, (c) $0.5s^{-1}$, (d) $1s^{-1}$.

*3.3 Research on sampling theory under different conditions*

*3.3.1 Influence of different strain rate and deformation temperature on sampling position*

Fig. 18(a) and (b) show the strain distribution in the deformation direction for samples under the conditions of $\varepsilon$=0.8, $\dot{\varepsilon} = 0.01s^{-1} \sim 1s^{-1}$, T=950°C$\sim$1100°C. Fig. 19 shows the distribution of sampling points with a distance of 0.125 mm between points.

Fig. 18 shows that the strain distributions decrease gradually from the center to the surface. At low strain rate of $0.01s^{-1}$, T=950°C$\sim$1100°C, the position of the compressed sample corresponding to the theoretical strain is about 0.398$\sim$0.407 of the distance from the center to the surface. Under the strain rate of $0.01s^{-1} \sim 1s^{-1}$, T=950°C$\sim$1100°C, the sampling position is located in the range of 0.465$\sim$0.512 from the center to the surface. This shows that the main factor of the sampling location is the strain rate, and the temperature has little effect on the sampling location.

Under the conditions of $\dot{\varepsilon} = 0.01s^{-1}$ and $\dot{\varepsilon} = 0.1s^{-1} \sim 1s^{-1}$, the 2/5 position and the 1/2 position of the distance from the center to the surface are the sampling point. As shown in Fig. 20, the error between the sampling point and the center and the preset strain of 0.8 in the range of 950°C$\sim$1100°C was analyzed. Under the conditions of $\dot{\varepsilon} = 0.01s^{-1}$ and $\dot{\varepsilon} = 0.1s^{-1} \sim 1s^{-1}$, the maximum errors between the central strain and the preset strain of 0.8 are 75% and 55%, respectively. Under the strain rate of $0.01s^{-1}$, the maximum error between the strain at 2/5 of the center and the preset strain of 0.8 is only 2.5%. Under the strain rate of $0.1s^{-1} \sim 1s^{-1}$, The maximum error between the strain at 1/2 of the center and the preset strain of 0.8 is 8.75%. The error range is always less than 10%, with high accuracy. It can be seen that, compared with the traditional sampling of the center of samples after hot compression, under the strain rate of $0.01s^{-1}$, the 2/5 position of the distance from the center to the surface corresponds to the preset strain, and under the strain rate of $0.1s^{-1} \sim 1s^{-1}$,the 1/2 position of the distance from the heart to the surface corresponds to the preset strain.
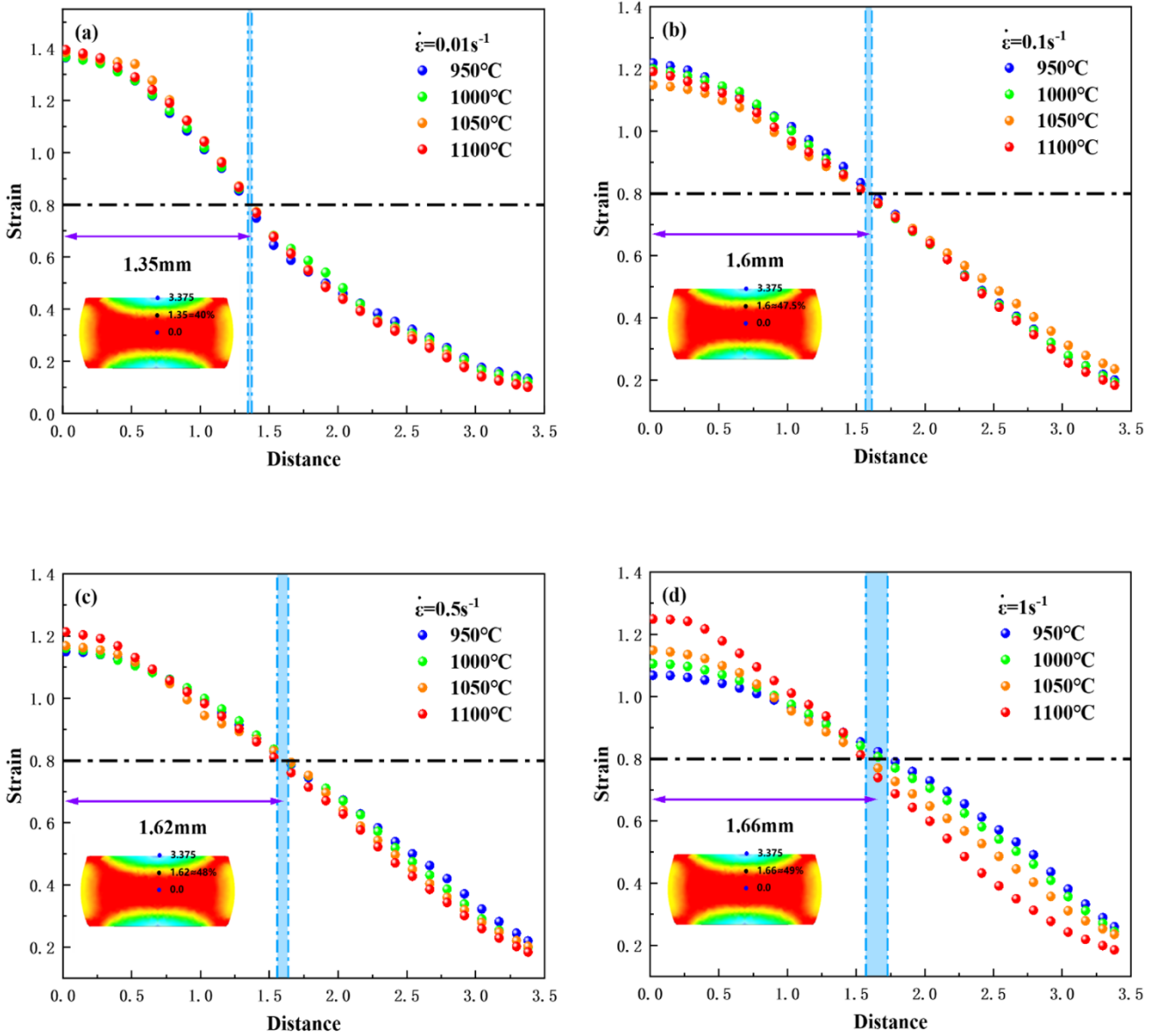
**Fig. 18.** Strain distribution from center to surface at different temperatures and strain rates.
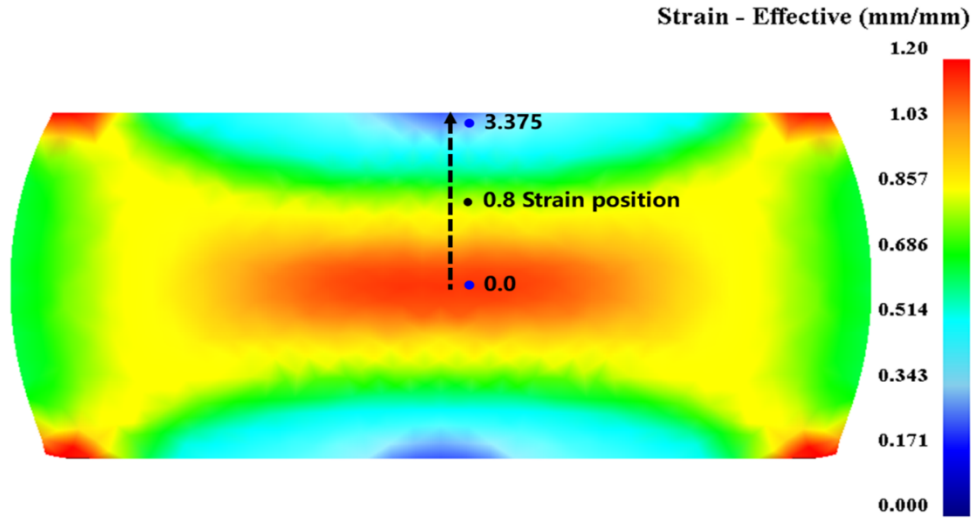
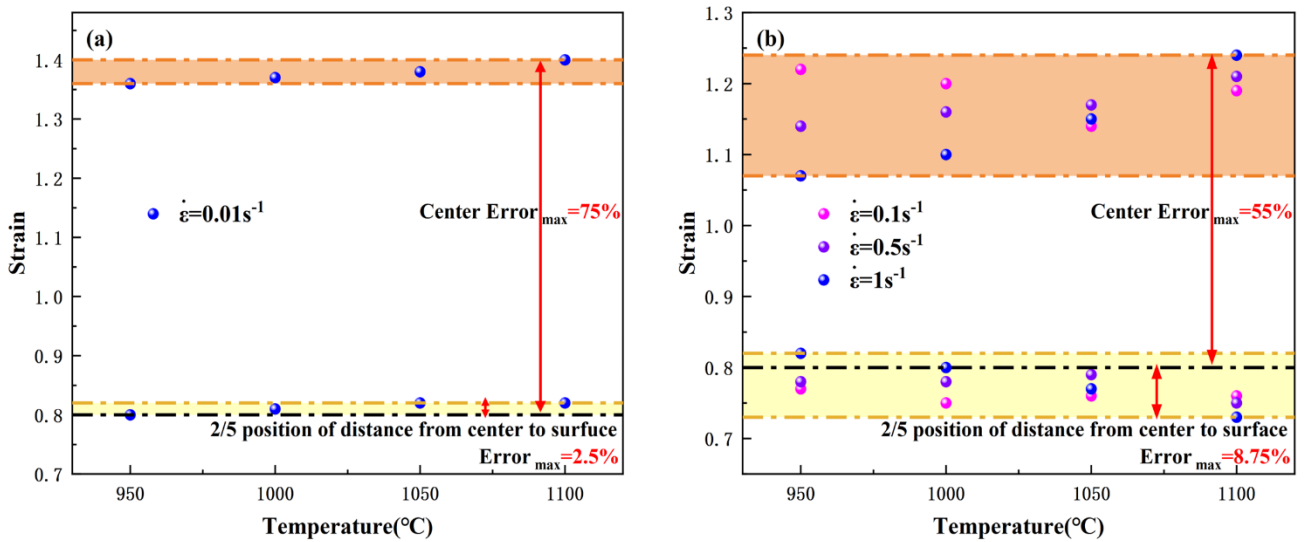**Fig. 19.** Schematic diagram of strain points in the compression direction (1050℃, 1s$^{-1}$).



**Fig. 20.** Error analysis under different sampling positions and preset strain of 0.8: (a) $\dot{\varepsilon} = 0.01s^{-1}$, T=950℃~1100℃, (b) $\dot{\varepsilon} = 0.1s^{-1} \sim 1s^{-1}$, T=950℃~1100℃.

*3.3.2 Influence of deformation amount on sampling position*

Fig. 21(a) and (b) show the strain distribution in the deformation direction for samples under the conditions of ε=0.51, $\dot{\varepsilon} = 0.01s^{-1} \sim 1s^{-1}$, T=950℃~1100℃. The trend of strain distribution is the same as that of different temperatures and strain rates, all decreasing gradually from the center to the surface. Under the conditions of $\dot{\varepsilon} = 0.01s^{-1}$ and $\dot{\varepsilon} = 0.1s^{-1} \sim 1s^{-1}$, the maximum errors between the central strain and the preset strain of 0.51 are 82% and 51%, respectively. Under the strain rate of $\dot{\varepsilon} = 0.01s^{-1}$, the maximum error between the strain at 2/5 of the center and the preset strain of 0.51 is 9.2%. Under the strain rate of $0.1s^{-1} \sim 1s^{-1}$, The maximum error between the strain at 1/2 of the center and the preset strain of 0.8 is only 4.1%, and the error range is always less than 10%.

Overall, it can be concluded that the above sampling method conforms the requirements for setting strain and can provide a more accurate data source for subsequent characterization experiments.
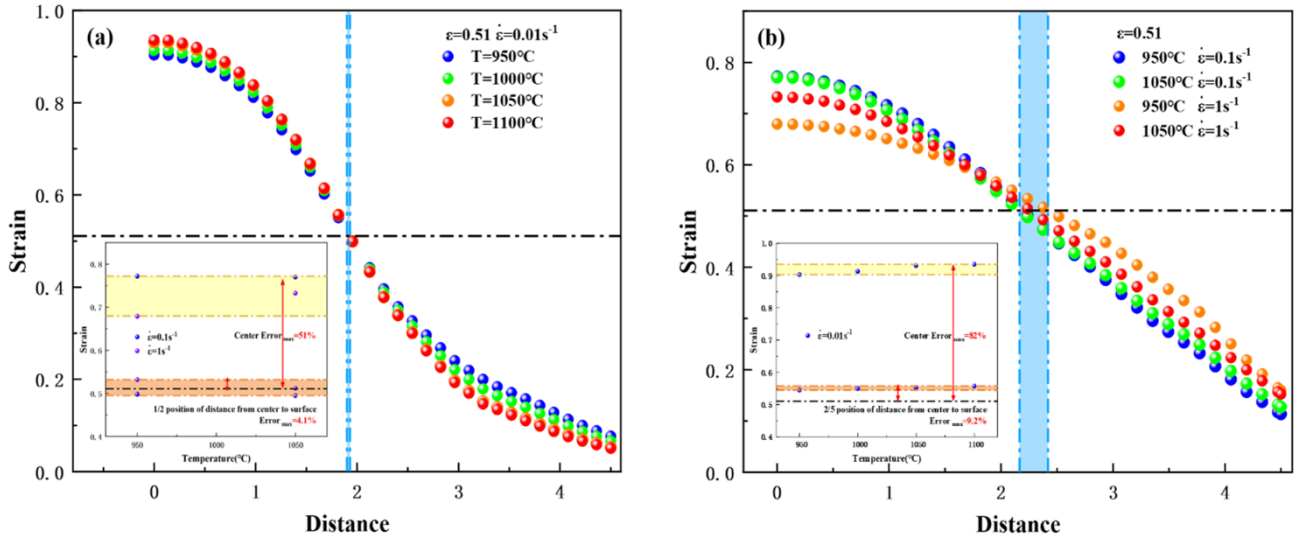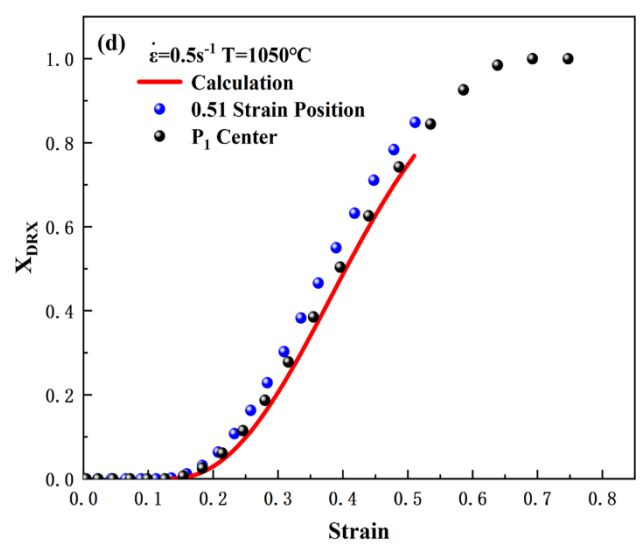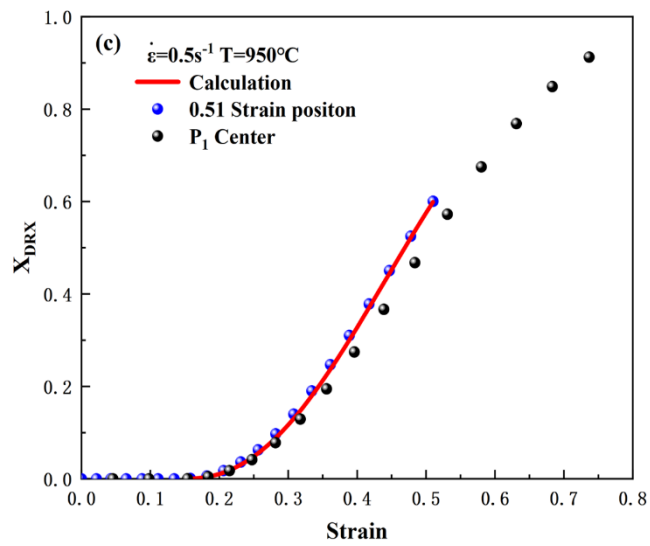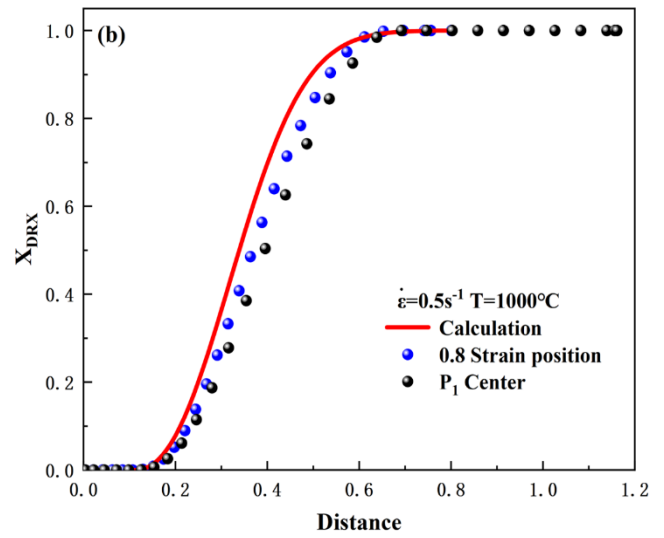
**Fig. 21.** Strain distribution from center to surface under ε=0.51: (a) $\dot{\varepsilon} = 0.01s^{-1}$, T=950°C~1100°C, (b) $\dot{\varepsilon} = 0.1s^{-1}$~$1s^{-1}$, T=950°C and 1050°C.

*3.4 Influence of theoretical strain position and center on $X_{DRX}$*

Fig. 22(a) and (b) analyze the dynamic recrystallization volume fraction of the theoretical strain position and the center under the condition of ε=0.8, $\dot{\varepsilon} = 0.5s^{-1}$, T=950°C. The two graphs do not highlight the advantage of accurately finding the preset strain position, because the material itself is prone to dynamic recrystallization. Before reaching the preset strain, two points have fully occurred dynamic recrystallization. However, it can be found that the strain at the center is 50% higher than the preset strain, which will continue to affect the grain refinement, resulting in deviation between the center structure and the actual situation. Furthermore, the preset strain remains closer to the actual DRX behavior than the center before full dynamic recrystallization.

By comparing Fig. 22(c), (d), (e), and (f), it can be seen that the importance of selecting an accurate sampling position is obvious with the deformation decreases. When the preset strain is 0.51 and 0.22, the pre-strain location not only fits the DRX kinetic model better, but also has an error of less than 8% with the DRX kinetic calculation model. The $X_{DRX}$ at the center position is larger than the calculated result of the DRX kinetic model, so the theory of observing the sample's center used to describe the DRX behavior of the preset strain is not accurate enough. The above accurate sampling theory provides the basis for subsequent microstructural characterization and analysis of the internal evolution of materials during thermomechanical deformation. It also provides accurate conditions for production to process better products.

(a) $\dot{\varepsilon}=0.5s^{-1}$ T=950℃
— Calculation
● 0.8 Strain position
● $P_1$ Center

(b) $\dot{\varepsilon}=0.5s^{-1}$ T=1000℃
— Calculation
● 0.8 Strain position
● $P_1$ Center

(c) $\dot{\varepsilon}=0.5s^{-1}$ T=950℃
— Calculation
● 0.51 Strain positon
● $P_1$ Center

(d) $\dot{\varepsilon}=0.5s^{-1}$ T=1050℃
— Calculation
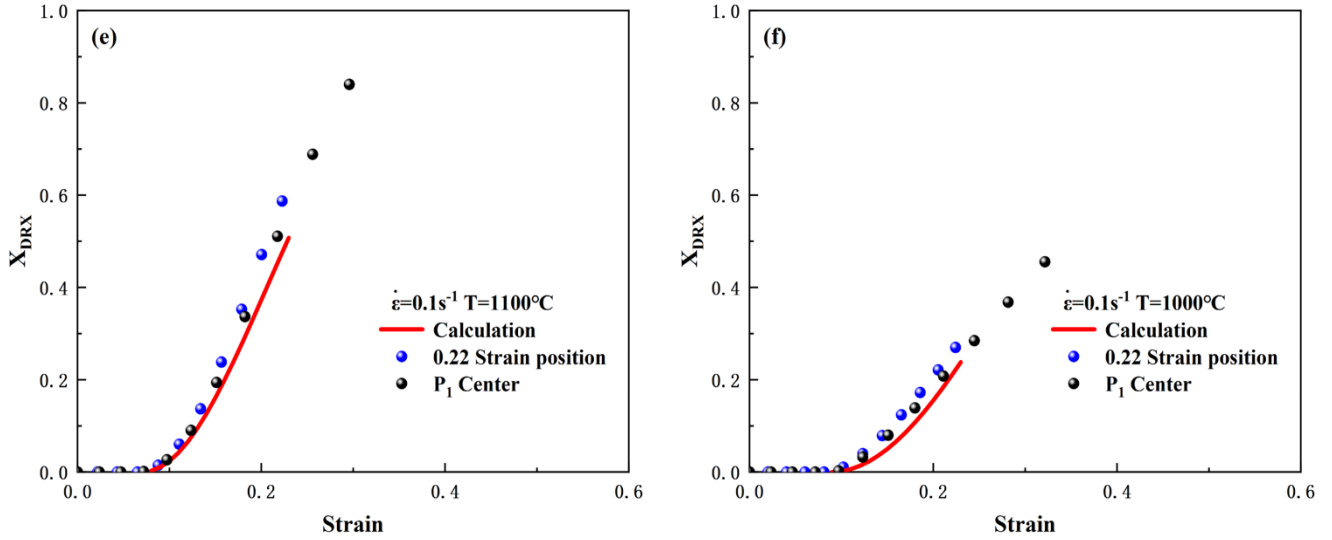● 0.51 Strain Position
● $P_1$ Center
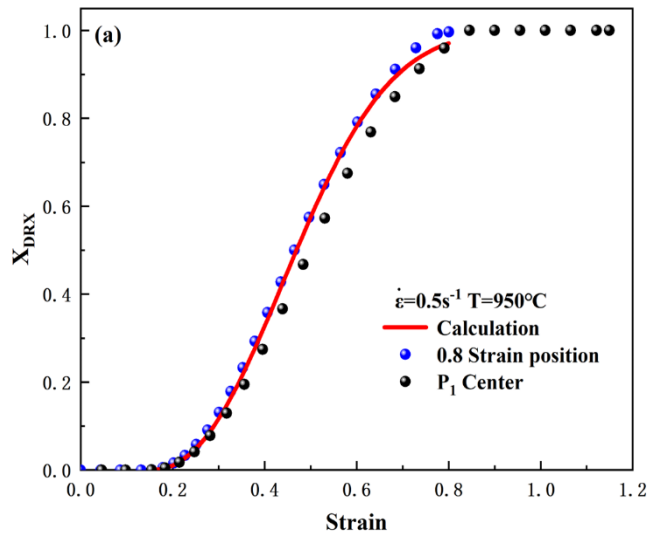
**Fig. 22.** Comparing the simulation results of the preset strain and the center position with the calculated values of the DRX dynamic model under different conditions:
(a) $\dot{\varepsilon} = 0.5s^{-1}$, T=950℃, ε=0.8, (b) $\dot{\varepsilon} = 0.5s^{-1}$, T=1000℃, ε=0.8, (c) $\dot{\varepsilon} = 0.5s^{-1}$, T=950℃, ε=0.51, (d) $\dot{\varepsilon} = 0.5s^{-1}$, T=1050℃, ε=0.51, (e) $\dot{\varepsilon} = 0.5s^{-1}$, T=1100℃, ε=0.22, (f) $\dot{\varepsilon} = 0.5s^{-1}$, T=1100℃, ε=0.22.

## 4 Conclusion

Based on physical simulation, this paper studies the flow stress curve of low carbon steel within the temperature range of 900℃~1100℃ and the strain rate of $0.01s^{-1}$~$1s^{-1}$. The internal mechanism of DRX behavior of the material is clarified, and DRX dynamic model suitable for different deformation conditions is established. The numerical simulation method reduces the sample's uniaxial cylindrical hot compression experiment and a theory is proposed to accurately describe the sampling position corresponding to the preset deformation during the actual processing. The main conclusions are as follows:

1) The deformation temperature and strain rate have a direct impact on the DRX behavior, and deformation conditions of high temperature and low strain rate will promote the DRX behavior of the material. The hot deformation activation energy of the material is 311.729KJ/mol calculated through the Zener-Hollomon model, and the relationship between the characteristic parameters of the material DRX behavior (peak stress $\sigma_p$, peak strain $\varepsilon_p$, critical stress $\sigma_c$, critical strain $\varepsilon_c$) and hot deformation parameters are revealed.

2) Based on the solution of the dynamic recovery coefficient $r$, the DRX kinetic model suitable for different deformation conditions is established. Comparing the predicted data with the experimental data shows a good matching in the range of 10%~90%, which verifies the accuracy of the model.

3) The numerical simulation method reduces the sample's uniaxial cylindrical hot compression experiment, which reveals and verifies the intrinsic mechanism of DRX behavior during high-temperature deformation of the material and the accuracy of the DRX kinetic model. Integrating the effects of multiple factors of deformation amount, deformation temperature and strain rate, a point analysis of the longitudinal axis of the hot compression sample is performed. A theory is proposed to accurately describe the sampling position corresponding to the preset deformation during the actual processing: under the strain rate of $0.01s^{-1}$, the 2/5 position of the distance from

the center to the surface corresponds to the preset strain, and under the strain rate of $0.1s^{-1} \sim 1s^{-1}$, the 1/2 position of the distance from the heart to the surface corresponds to the preset strain. Comparing the simulation results of the preset strain and the center position with the calculated values of the DRX kinetic model under different conditions to verify the importance of finding the accurate sampling location.

**CRediT authorship contribution statement:**

**Yan Peng**: Conceptualization, Funding acquisition, Supervision, Writing - review & editing. **Shicheng Liang**: Conceived, Designed, Performed the experiments, Visualization, Formal analysis, Investigation, Writing - original draft. **Caiyi Liu**: Formal analysis, Writing - review & editing. **Silvia Barella**: Investigation, Data curation. **Shuo Guo**: Experiments. **Andrea Gruttadauria**: Experiments. **Marco Belfi**: Experiments. **Yang Liu**: Experiments. **XiaoBo Qu**: Experiments. **Carlo Mapelli**: Investigation, Formal analysis.

**Declaration of competing interest:**

The authors declare that they have no known competing financial interests or personal relationships that could have appeared to influence the work reported in this paper.

**Reference**

[1] K Huang, R E Logé. A Review of Dynamic Recrystallization Phenomena in Metallic Materials [J]. Materials & Design, 2016, 111: 548-574.

[2] Y C Lin, X M Chen. A Critical Review of Experimental Results and Constitutive Descriptions for Metals and Alloys in Hot Working [J]. Materials & Design, 2011, 32(4): 1733-1759.

[3] Y Q Ning, B Y Zhang. Hot Forming of Superalloy Parts and Structures [J]. Encyclopedia of Materials: Metals and Alloys, 2022, 435-437.

[4] A Chamanfar, M T Alamoudi, et al. Analysis of flow stress and microstructure during hot compression of 6099 aluminum alloy (AA6099) [J]. Materials Science and Engineering: A, 2019, 743: 684-696.

[5] X T Zhong, L Wang, et al. Transition of Dynamic Recrystallization Mechanism During Hot Deformation of Incoloy 028 Alloy [J]. Journal of Materials Science & Technology, 2020, 42: 241-253.

[6] K Ma, Z Y Liu, et al. Microstructure Evolution and Hot Deformation Behavior of Carbon Nanotube Reinforced 2009Al Composite with Bimodal Grain Structure [J]. Journal of Materials Science & Technology, 2021, 70: 73-82.

[7] Y. C. Lin, M.-S. Chen, J. Zhong, Comput. Mater. Sci. 2008, 43, 1117.

[8] G. R. Johnson. Proc. 7th Inf. Symp. Ballistics,, The Hague 1983, p. 541.

[9] C. M. Sellars, W. J. Mctegart, Acta Metall. 1966, 14, 1136.

[10] Q. Wang, N. Ma, M. Takahashi, X. Luo, C. Li, Acta Mater. 2020, 199, 326.

[11] C M Li, L Huang, et al. Influence of Hot Deformation on Dynamic Recrystallization Behavior of 300M Steel: Rules and modeling [J]. Materials Science and Engineering: A, 2020, 797.

[12] M S Chen, Y C Lin, et al. The Kinetics of Dynamic Recrystallization of 42CrMo Steel [J]. Materials Science and Engineering: A, 2012, (556): 260-266.

[13] M J Wang, C Y Sun, et al. Experimental Investigations and Constitutive Modeling of the Dynamic Recrystallization Behavior of Inconel 740 Superalloy [J]. Materials Science and Engineering: A, 2020, 793.

[14] J D Li, J S Liu, et al. Strain Compensation Constitutive Model and Parameter Optimization for Nb-Contained 316LN [J]. Metals, 2019, 9(2): 212.

[15] Y W Xu, D Tang, et al. Dynamic Recrystallization Kinetics Model of X70 Pipeline Steel [J]. Materials & Design, 2012, 39: 168-174.

[16] L Chen, W Y Sun, et al. Modelling of Constitutive Relationship, Dynamic Recrystallization and Grain Size of 40Cr Steel During Hot Deformation Process [J]. Results in Physics, 2019, 12: 784-792.

[17] H Wu, M X Liu, et al. Experimental Study and Numerical Simulation of Dynamic Recrystallization for a FGH96 Superalloy During Isothermal Compression [J]. Journal of Materials Research and Technology, 2020, 9(3): 5090-5104.

[18] H C Ji, Z S Peng, et al. Characterization of the Microstructures and Dynamic Recrystallization Behavior of Ti-6Al-4V Titanium Alloy through Experiments and Simulations [J]. Journal. of Materials Engineering and Performance, 2021, 30: 8257–8275.

[19] X Y Feng, X P, et al. Deformation Behavior and Dynamic Recrystallization of Mg-1Li-1Al Alloy [J]. Metals, 2021, 11(11): 1696.

[20] M H Marzbali, H R Jafarian, et al. On the Microstructure and Mechanical Properties of FeCoCrCuNi High Entropy Alloy During Hot Compression [J]. Journal of Materials Research and Technology, 2022, 16: 1747-1760.

[21] X Y Sun, M Zhang, et al. Kinetics and Numerical Simulation of Dynamic Recrystallization Behavior of Medium Mn Steel in Hot Working [J]. Steel Research International, 2020, 91(7).

[22] K C Nayak, P P Date. Physical Simulation of Hot Rolling of Powder Metallurgy-Based Al/SiC Composite by Plane Strain Multi Stage Compression [J]. Materials Characterization, 2021,173.

[23] H Wang, G L Qin, et al. A Modified Arrhenius Constitutive Model of 2219-O Aluminum Alloy Based on Hot Compression with Simulation Verification [J]. Journal of Materials Research and Technology, 2022,19: 3302-3320.

[24] H C Ji, Z M Cai, et al. DRX Behavior and Microstructure Evolution of 33Cr23Ni8Mn3N: Experiment and Finite Element Simulation [J]. Journal of Materials Research and Technology, 2020, 9(3): 4340-4355.

[25] J Zhao, Z H Wang, et al. FEM Analysis and Experimental Study of Deformation Nonuniformity After Hot Compression [J]. Steel, 2007, (12): 53-56.

[26] F Sui, Y Zuo, et al. Determination of the Observation Area for Metallographic Microstructure of GH4033 Superalloy in a Uniaxially Thermo-Mechanical Compression Experiment [J]. Acta Metall. Sin. (Engl. Lett.), 2014,27: 494-500.

[27] X J Ye, X J Gong, et al. Deformation Inhomogeneity Due to Sample–Anvil Friction in Cylindrical Compression Test [J]. Transactions of Nonferrous Metals Society of China, 2019, 2: 279-286.

[28] E I Poliak, J J Jonas. A One-Parameter Approach to Determining the Critical Conditions for the Initiation of Dynamic Recrystallization [J]. Acta Materialia, 1996, 44: 127-136.

[29] H. Mirzadeh, A. Najafizadeh. Prediction of the Critical Conditions for Initiation of Dynamic Recrystallization [J]. Materials & Design, 2010, 31: 1174-1179.

[30] E I Poliak, J J Jonas. Initiation of Dynamic Recrystallization in Constant Strain Rate Hot Deformation [J]. ISIJ International, 2003, 43:692-700.

[31] G W Zhou, Z H Li, et al. A Polycrystal Plasticity based Discontinuous Dynamic Recrystallization Simulation Method and its Application to Copper [J]. International Journal of Plasticity, 2017, 91: 48-76.

[32] B S Xie, Q W Cai, et al. A New Constitutive Model for the High-Temperature Flow Behavior of 95CrMo Steel [J]. Journal of materials engineering and performance, 2016, 25(12): 5127-5137.

[33] S A Sajadi, M R Toroghinejad, et al. A Study of Hot Compression Behavior of an As-Cast FeCrCuNi2Mn2 High-Entropy Alloy [J]. Journal of Alloys and Compounds, 2022, 896.

[34] C Zener, J H Hollomon. Effect of Strain Rate Upon Plastic Flow of Steel [J]. Journal of Applied Physics, 1944, 15(1):22-32.

[35]  Y T Wang, J B Li, et al. Effect of Zener–Hollomon Parameter on Hot Deformation Behavior of CoCrFeMnNiC$_{0.5}$ High Entropy Alloy [J]. Materials Science and Engineering: A, 2019: 138483

[36]  X Wang, K Chandrashekhara, et al. Modeling and Simulation of Dynamic Recrystallization Behavior in Alloyed Steel 15V38 during Hot Rolling [J]. Steel Research International, 2019, 90(4).

[37]  H L Wei, G Q Liu, et al. Dynamic Recrystallization Behavior of a Medium Carbon Vanadium Microalloyed Steel [J]. Materials Science and Engineering: A, 2013, 573: 215-221.

[38]  J J Jonas, X Quelennec, et al. The Avrami Kinetics of Dynamic Recrystallization [J]. Acta Materialia, 2009, 57(9): 2748-2756.

[39]  C Y Liu, Y Peng, et al. Characterization of Dynamic Recrystallization Behavior of Low Carbon Steel Under Flexible Rolling Process [J]. Materials Today Communications, 2021, 29: 102777

[40]  S L Wang, M X Zhang, et al. Study on the Dynamic Recrystallization Model and Mechanism of Nuclear Grade 316LN Austenitic Stainless Steel [J]. Materials Characterization, 2016, 118: 92-101.

[41]  R Luo, L L Chen, et al. Characteristic and Mechanism of Dynamic Recrystallization in a Newly Developed Fe-Cr-Ni-Al-Nb Superalloy During Hot Deformation [J]. Journal of Alloys and Compounds, 2021, 865: 158601.

[42]   J. R. C. Guimaraes, P. R. Rios, A. L. M. Alves, Mater. Res. 2019, 22,2748.

[43]  S M Hussaini, S K Singh, et al. Experimental and Numerical Investigation of Formability for Austenitic Stainless Steel 316 at Elevated Temperatures [J]. Journal of Materials Research and Technology, 2014, 3(1): 17-2.

[44]  X C Li, L L Duan, et al. Experimental Study and Numerical Simulation of Dynamic Recrystallization Behavior of a Micro-alloyed Plastic Mold Steel [J]. Materials & Design(1980-2015), 2015, 66: 309-320.

[45]  H L Ding, T Y Wang, et al. FEM Modeling of Dynamical Recrystallization During Multi-Pass Hot Rolling of AM50 Alloy and Experimental Verification [J]. Transactions of Nonferrous Metals Society of China, 2013, 23(9): 2678-2685.

[46]  P H Geng, G L Qin, et al. Characterization of Microstructures and Hot-Compressive Behavior of GH4169 Superalloy by Kinetics Analysis and Simulation [J]. Journal of Materials Processing Technology, 2021, 288: 116879.

[47]  R C Buckingham, C Argyrakis, et al. The Effect of Strain Distribution on Microstructural Developments During Forging in a Newly Developed Nickel Base Superalloy [J]. Materials Science and Engineering: A, 2016, 654: 317-328.